Environmental Nanotechnology, Monitoring & Management 20 (2023) 100818

Contents lists available at ScienceDirect

Environmental Nanotechnology, Monitoring & Management

journal homepage: www.elsevier.com/locate/enmm

Isotherm, kinetics, thermodynamics, recyclability and mechanism of ultrasonic assisted adsorption of methylene blue and lead (II) ions using green synthesized nickel oxide nanoparticles

Dominic Chukwu Onu [a,g,h], Akinpelu Kamoru Babayemi [a,h], Titus Chinedu Egbosiuba [a,h,*], Blessing Onyinye Okafor [a,h], Ijeoma Jacinta Ani [b,h], Saheed Mustapha [c], Jimoh Oladejo Tijani [c], Wisdom Chukwuemeke Ulakpa [d], Prosper Eguono Ovuoraye [e], Ambali Saka Abdulkareem [f]

[a] Department of Chemical Engineering, Chukwuemeka Odumegwu Ojukwu University, P.M.B 02, Uli Campus, Anambra State, Nigeria
[b] Caritas University Amorji-Nike, P.M.B 01784, Emene, Enugu State, Nigeria
[c] Department of Chemistry, Federal University of Technology, P.M.B 65, Minna, Niger State, Nigeria
[d] Department of Chemical and Petroleum Engineering, Delta State University of Science and Technology, P.M.B 05, Ozoro, Delta State, Nigeria
[e] Department of Chemical Engineering, Federal University of Petroleum Resources, P.M.B 1221 Effurun, Delta State, Nigeria
[f] Department of Chemical Engineering, Federal University of Technology, P.M.B 65, Minna, Niger State, Nigeria
[g] Department of Chemical Engineering, Federal Polytechnic, P.M.B 21, Oko Anambra State, Nigeria
[h] Nanotechnology Research Group, Chukwuemeka Odumegwu Ojukwu University, P.M.B 02, Uli Campus, Anambra State, Nigeria

ARTICLE INFO

Keywords:
Nickel oxide nanoparticles
Methylene blue
Lead (II) ions
Psidium guajava leaves extract
Adsorption mechanism

ABSTRACT

One of the urgent global problems demanding effective mitigation strategies is the pollution caused by organic dyes and metal ions like methylene blue and lead (II) ions. In recent times, the increasing applications of nickel oxide nanoparticles in biomedicine, catalysis, sensors in optoelectronic materials, and the prevention of environmental pollution have attracted researchers' interest across the globe. Herein, *Psidium guajava* leaves extract was utilized to synthesize green nickel oxide nanoparticles (PG-NiONPs). Surface and analytical techniques were employed to characterize PG-NiONPs and were thereafter applied to remove methylene blue and lead (II) ions from wastewater. The results revealed the quantified presence of phytochemicals such as alkaloids, phenols, tannins, flavonoids and saponins in the *Psidium guajava* leaves extract. The prepared PG-NiONPs revealed a crystalline phase, functional groups, mesoporous and microstructural arrangements typical of nickel oxide nanoparticles. The surface area of PG-NiONPs was obtained as 85.40 m^2/g. The best ultrasonic-assisted adsorption of MB and Pb(II) ions was achieved at pH values of 6 and 5 for MB and Pb(II), a contact time of 60 min, an adsorbent mass of 40 mg/L, and a temperature of 50 °C, respectively. The maximum MB and Pb(II) adsorption capacities of 495.58 and 508.56 mg/g were evaluated. The experimental data corroborated with the pseudo-second-order and Toth isotherm models. The adsorption of MB and Pb(II) over green PG-NiONPs was a thermodynamically spontaneous process. The PG-NiONPs indicated good recyclability with high stability even after 8 adsorption cycles. Overall, the PG-NiONPs is a potential adsorbent for improved toxic dyes, metal ions and other scavengers removal from wastewater.

1. Introduction

The health of the global environment is heavily burdened by industrialization and population increase. Consequently, there is an alarming increase in the discharge of untreated developing contaminants such as dyes and metal ions into water sources from the textile, battery, electroplating, and ceramic industries (Kovo et al., 2023; Sagadevan et al., 2022). According to a recent study, roughly 10,000 different types of commercial dyes totalling 700,000 tons are manufactured worldwide each year (Noukelag et al., 2021; Tran et al., 2022). Dyes and metal ions discharged into the environment from textile and battery industries, including methylene blue (MB) and lead (Pb)(II), are highly toxic, environmentally persistent, carcinogenic, and mutagenic, thereby endangering the ability of aquatic animals to reproduce and

* Corresponding author at: Department of Chemical Engineering, Chukwuemeka Odumegwu Ojukwu University, P.M.B 02, Uli Campus, Anambra State, Nigeria.
E-mail address: ct.egbosiuba@coou.edu.ng (T. Chinedu Egbosiuba).

https://doi.org/10.1016/j.enmm.2023.100818
Received 6 December 2022; Received in revised form 28 February 2023; Accepted 26 March 2023
Available online 1 April 2023

thrive (Lingamdinne et al., 2020, 2016; Sagadevan et al., 2022). Dye-contaminated wastewater hinders direct sunlight penetration and increases surface waters' abnormal coloration (Egbosiuba, 2022a; Egbosiuba, 2022c; Lingamdinne et al., 2018). Skin and eye injuries can result from exposure to MB while ingesting it directly can induce a fast heart rate, vomiting, digestive problems, tissue necrosis, and nausea (Adel et al., 2022; Egbosiuba et al., 2020a; Egbosiuba et al., 2020b). On the other hand, wastewater containing heavy metal ions, such as Pb(II), seriously pollutes the environment. Chronic exposure to lead pollution can have negative effects on human health, including nervous disorders, memory loss, plumbism, nausea, diarrhea, convulsions, cardiovascular problems, brain abnormalities, and even death (Egbosiuba et al., 2022; Lingamdinne et al., 2023; Lingamdinne et al., 2022). Therefore, it is critically necessary to enhance wastewater treatment technology to effectively separate MB and Pb(II) from wastewater.

Several purification techniques, including improved oxidation (Khare et al., 2021), ion exchange (Khare et al., 2021), membrane technology (Mustapha et al., 2023), coagulation (Onukwuli et al., 2021), photocatalysis (Tijani et al., 2022; Tijani et al., 2021), biodegradation (Ahmed et al., 2021), and adsorption (Sagadevan et al., 2022) approach, have been reported for the efficient removal of organic dyes and heavy metals from wastewater. Given their affordability, ease of reuse, and environmental friendliness, adsorption is the most extensively utilized method (Roy et al., 2022). The development of an adsorbent with a good adsorption performance, practical application potential, high stability, and significant regeneration capacity is very vital in adsorption technology (Kavand et al., 2020). Particularly, the limited adsorption capacity of the adsorbents lengthens the removal time and increases the costs of operation. In addition, the lack of adsorption site availability on the adsorbent surface surrounding is the primary limiting factor resulting in low adsorption capacity (Uko et al., 2022). Before now, biochar, activated carbons, zeolites, metal–organic frameworks, nanoparticles, and nanocomposites are just a few of the effective materials that have been developed by researchers to remove dyes molecules and metal ions by adsorption processes (Egbosiuba, 2022a; Egbosiuba, 2022c; Gómez-Avilés et al., 2022; Tao et al., 2022). These adsorbents have recorded good adsorption performance, but a certain amount of hazardous chemicals are needed for the synthesis of the adsorbent materials, thus raising the danger of secondary pollution (Tran et al., 2022). Consequently, the environmentally friendly production of nanoparticles has drawn a lot of interest (Tran et al., 2022). Numerous studies suggested that natural components of plant extracts could function as reducing and stabilizing agents during the synthesis of nanoparticles (Ali et al., 2022; Riaz et al., 2022).

Psidium guajava (Guava) plant belongs to the *Myrtaceae* family and is grown principally in tropical areas such as India, Indonesia, South America, Pakistan, and Nigeria due to its different medicinal and nutritive benefits. Different parts of the guava plant, including leaves, roots, stems, bark, shoots, and fruits, have been employed for ethnomedicinal purposes, especially in treating dysentery, hypertension, stomach ache, diabetes, gastroenteritis, diarrhea, and pain relief (Ekeleme et al., 2017). *Psidium guajava* leaves are characteristically dark green in colour, with an oval, elliptical, and obtuse-type apex. Among all the parts of *Psidium guajava*, leaves are the largest accumulators of bioactive compounds of secondary metabolites. Although *Psidium guajava* leaves are considered agricultural waste, their extracts are a rich source of phytochemicals. Furthermore, the phytochemical screening undertaken by previous researchers has disclosed that *Psidium guajava* contains bioactive compounds such as alkaloids, flavonoids, tannins, phenolics, saponins, terpenoids and glucosides (Kumar et al., 2021; Oncho et al., 2021). In nanotechnology applications, the biomolecules serve as a reducing and stabilizing agent in the green synthesis of metallic nanoparticles. For instance, *Psidium guajava* leaf extract was used to synthesize silver nanoparticles for antibacterial activity (Venugopal, 2017). In 2021, Zayed et al. (Zayed et al., 2021) prepared zinc oxide nanoparticles using *Psidium guajava* leaves extract which was subsequently doped with chitosan for the coating of cotton fabrics. In addition, a monoclinic symmetry of copper oxide nanoparticles with a particle size of ~ 33 nm was prepared using *Psidium guajava* leaves extract (Varughese et al., 2020).

At the moment, the production of nickel oxide nanoparticles through a green method is increasingly attracting interest. Even though different plant extracts were used to make green nickel oxide nanoparticles, their specific uses were either not described or were only briefly mentioned in the literature. For instance, Zhang et al. (Zhang et al., 2021) prepared cubic and spherical nickel oxide nanoparticles of 9.1 nm from *Eichhornia crassipes* extract for fermentative hydrogen production. In another study, nickel oxide nanoparticles of 9.6 nm average size were synthesized by a green procedure using medicinal flower extract of *Clitoria ternatea* for antibacterial and photocatalytic degradation application (Prabhu et al., 2022). Also, nickel oxide nanoparticles were developed by an environmentally friendly method using orange leaf extract for biomedical applications and antibacterial activity (Khodair et al., 2022). Another study prepared cubic structural spherical nickel oxide nanoparticles of an average diameter of 10 to 15 nm using Zea mays lea silk aqueous extract for electrochemical energy storage device applications (Nwanya et al., 2020). However, these studies utilized the prepared nickel oxide nanoparticles for photocatalytic, biomedical, antibacterial and electrochemical sensing purposes. As a result, expanding the applications of green synthesized nickel oxide nanoparticles in the adsorptive removal of dyes and metal ions from the environment is critical. To the best of our knowledge, this is the first study to report the green synthesis of nickel oxide nanoparticles using *Psidium guajava* leaf extract for the mitigation of methylene blue and lead (II) ions from wastewater.

In this study, the phytochemical constituents of *Psidium guajava* leaf extract were determined qualitatively and quantitatively for the bioactive compound's capacity as a reducing, capping, and stabilizing agents. The *Psidium guajava* leaves extract was used to facilitate the green synthesis of nickel oxide nanoparticles in the present work. The biomolecules such as alkaloids, phenols, tannins, flavonoids, saponins and terpenoids prevent the aggregation of nickel oxide nanoparticles and enhance the surface area and functionality of the nanoparticles. The prepared nickel oxide nanoparticles were also characterized using X-ray diffraction, Fourier transform infrared spectroscopy, high-resolution scanning electron microscopy, Energy-dispersive, high-resolution transmission electron microscopy, Thermogravimetric, and Brunauer Emmett Teller methods. In the adsorptive removal of methylene blue and lead (II) ions, the effect of pH, contact time, nanoadsorbent mass, and temperature were investigated. The nature of the dye and metal ion adsorption was clarified using the kinetic, isotherm, and thermodynamic models. The recyclability and the stability of the nanoadsorbent were also evaluated, while the adsorption mechanisms were also proposed in this work.

2. Materials and methods

2.1. Materials

The chemicals used in this study are sodium hydroxide (NaOH), tetraoxosulphate (VI) acid (H_2SO_4), nitric acid (HNO_3), nickel chloride hexahydrate ($NiCl_2{\cdot}6H_2O$), methylene blue (MB) and lead (II) ions, purchased from Sigma Aldrich, Lagos Nigeria. All the chemicals were of analytical grade (percentage purity range of 95–99.9 %) and were used as received without further purification. Distilled water was used in this study for all solution preparations. Guava (*Psidium guajava*) leaves were obtained from Neni, Anaocha Anambra State, Nigeria.

2.2. Methods

The detailed experimental techniques used in the biosynthesis of nickel oxide nanoparticles, characterization of the nanoparticles, evaluation of Methylene blue (MB) and lead (II) ions concentration in

wastewater and batch adsorption study to effectively remove the dye molecules and metal ions pollutants from wastewater are described in the following section.

2.2.1. Preparation of Psidium guajava (PG) leaves extract

Fresh guava leaves, *Psidium guajava* (PG, 100 g), were cleaned with deionized water to eliminate dust and surface pollutants before being dried in the laboratory for 14 days at ambient temperature (25 to 30 °C). An electric blender (Century, 1406) was used to grind the dried PG leaves into powder before the determination of the phytochemical constituents of PG leaves extract. Biomolecules such as flavonoids, saponins, alkaloids, steroids, tannins, and terpenoids that function as reducing and stabilizing agents were evaluated qualitatively and quantitatively using standard procedures reported elsewhere with minor modifications (Bouabid et al., 2020; Egbosiuba et al., 2021a; Kunatsa et al., 2020).

To make the PG leaf extract, 25 g of powdered PG leaves samples were weighed into a 1000 mL conical flask with 250 mL deionized water and heated on the magnetic stirrer (150 rpm) for 20 min at 80 °C to liberate the phytochemicals from the leaves tissues. After that, the sample was allowed to cool to ambient temperature before being filtered through the Whatman number 1 filter paper. The filtrate was labelled PG-extract and kept refrigerated until further use to avoid any detrimental effects on the extract.

2.2.2. Green synthesis of nickel oxide nanoparticles

Initially, 5.94 g nickel chloride hexahydrate ($NiCl_2{\cdot}6H_2O$, 0.1 M) was measured into a 500 mL conical flask holding 250 mL deionized water to make nickel oxide nanoparticles. To obtain a homogeneous solution, the mixture was repeatedly agitated. The salt solution was then placed on a magnetic stirrer (150 rpm) at 60 °C to reach a consistent temperature before adding 25 mL of PG-extract. The pH of the iron salt and PG-extract mixture was then adjusted to 8 by adding 5 mL NaOH (0.5 M) dropwise and allowing it to stable for 30 min. Following that, the color of the reaction mixture changed from dark green to brown, suggesting the formation of nickel oxide nanoparticles. After cooling to ambient temperature, the mixture was washed numerous times with ultra-pure water and ethanol to produce a pH of approximately 7. Finally, the mixture was filtered using Whatman no. 1 filter paper, and the resulting residue was dried in a**n** oven **at** 105 °C for 12 h. To eliminate residual moisture, impurities, and chlorides, the dried nickel oxide nanoparticles were calcined in a muffle furnace at 600 °C for 6 h. The produced nickel oxide nanoparticles were labelled PG-NiONPs and stored in an airtight bottle until they could be characterized and used in adsorption tests. The preparation procedures for PG-NiONPs are schematically described in Fig. 1.

2.2.3. Characterization of PG-NiONPs

The structure and phase of PG-NiONPs were determined by X-ray diffraction (XRD) examination on a Shimadzu Scientific, 6000 utilizing Cu-Ka radiation at 1.5406 nm. In addition, the functional groups present on the PG-NiONPs were determined using Fourier transform infrared spectroscopy (FTIR, PerkinElmer, UK). Using high-resolution scanning electron microscopy (HRSEM, Zeiss Auriga, UK) and high-resolution transmission electron microscopy (HRTEM, Zeiss Auriga, UK), the surface morphological and microstructural features of the PG-NiONPs were further evaluated. Thermogravimetric analysis was used to determine the thermal stability of the generated iron oxide nanoparticles (TGA, Q600, USA). The surface areas and porous architectures of the PG-NiONPs were also investigated using the Brunauer Emmett Teller

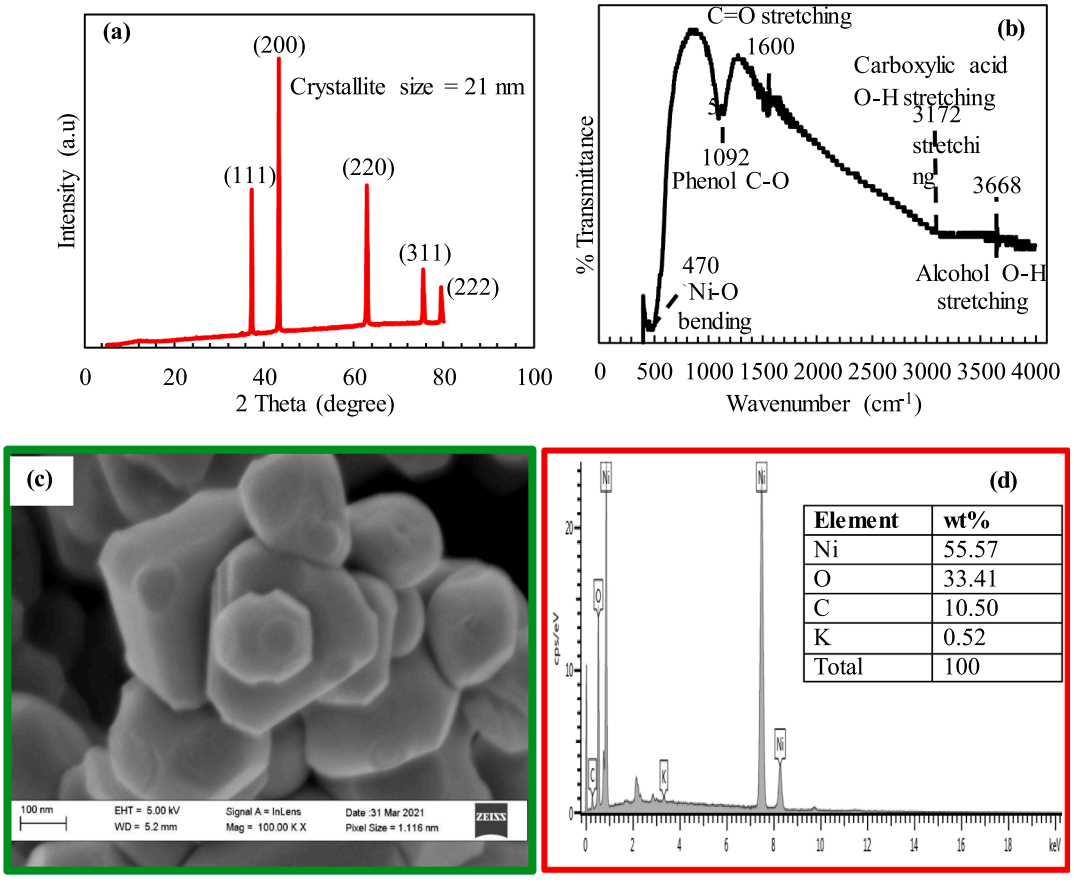

Fig. 1. Schematic representation of the green synthesis of PG-NiONPs. (For interpretation of the references to color in this figure legend, the reader is referred to the web version of this article.)

(BET, NOVA4200e, Quantachrome UK) method.

2.2.4. Analysis of MB and Pb(II) ion

Herein, textile and battery industry wastewater were procured from the industrial clusters at Nnewi, Anambra, Nigeria. The MB and Pb(II) concentrations in the wastewater were determined as 52 and 34 mg/g using a PerkinElmer UV–Vis spectrophotometer at a wavelength of 664 nm and atomic adsorption spectrometry (AAS, PG 990, PG Instruments, UK). In addition, a 1000 mg/L stock solution of MB and Pb(II) ions was prepared to achieve serial dilutions to the initial concentrations of 20, 50, and 100 mg/L used in this study. Overall, the supernatants were prepared in the ultrasonic bath (SB25-12DT, Scientz) before being filtered through the Whatman grade 1 filter paper. Thereafter, the residual concentrations of the MB and Pb(II) in the filtrate were assessed using a UV–Vis spectrometer and the AAS technique.

2.2.5. Batch adsorption study

Using the following approach, the ultrasonic-assisted adsorption performance of PG-NiONPs for MB and Pb(II) ions was investigated under the influence of pH, contact time, nanoadsorbent mass, and temperature. By measuring 5 mg/L of PG-NiONPs into a conical flask of 250 mL containing 100 mL of the MB/Pb(II) solution at a contact time and temperature of 20 min and 25 °C, the pH of the solution was adjusted in the range of 2 to 10 using 1 M HCl and 1 M NaOH. The mixture was agitated using an ultrasonic bath (250 rpm) to achieve an adequate adsorption process. Thereafter, the PG-NiONPs were removed from the solution, filtered using Whatman grade 1 filter paper, and the filtrate was analyzed using a UV–Vis spectrophotometer and AAS method for the residual concentrations of MB and Pb(II) ions, respectively. Specifically, Eq. (1) was used to calculate the removal efficiency (R, %) of PG-NiONPs towards MB/Pb(II), whereas Eq. (2) was used to calculate the equilibrium adsorption capacity (qe, mg/g) (Bhaumik et al., 2021).

$$R\,(\%) = \left(\frac{C_0 - C_e}{C_0}\right) x\,100 \tag{1}$$

$$q_e\,(mg/g) = \left(\frac{C_0 - C_e}{m}\right) x\,V \tag{2}$$

where C_0 (mg/L) and C_e (mg/L) are the initial and equilibrium concentrations of MB and Pb(II), respectively, and V (mL) and m (mg/L) are the volume of MB/Pb(II) solution used and the amount of PG-NiONPs, respectively.

The effects of other adsorption parameters, such as contact time (10, 20, 30, 40, 50, 60, 90, 120, 180, and 240 min) at various initial concentrations of MB/Pb(II) solution (50, 75, and 100 mg/L) and nanoadsorbent mass (5, 10, 15, 20, 25, 30, 35, 40, 45, and 50 mg/L) at different temperatures (30, 40, and 50 °C) on the adsorption process, were also investigated using the same procedure reported earlier The adsorption data were replicated three times for each parameter adjustment to ensure repeatability.

Adsorption kinetic (pseudo-first order, pseudo-second order, and Elovich) models, adsorption isotherm (Langmuir, Freundlich, and Temkin) models, and adsorption thermodynamics were used to match the data from batch tests.

2.2.6. Recyclability and stability

The cycle performance of nickel oxide nanoparticles was assessed using adsorption–desorption assays, which involved introducing 40 mg/L of PG-NiONPs to a 100 mg/L of MB/Pb(II) solution and stirring continuously at 150 rpm for 3 h at 50 °C. To evaluate the cycle performance, the reusability of nickel oxide nanoparticles was tested using 1 M each for both NaOH and HCl with 8 repetitions. The desorption efficiency (DE) of the nanoadsorbents was calculated using Eq. (S1) (Tao et al., 2022).

2.2.7. Statistical data analysis

The coefficient of determination (R^2) and the chi-square (χ^2) are mathematically indicated in Eqs. (3) and (4) (Wang and Guo, 2020) were used to further validate and compare the accurate fitting of the experimental data to the isotherm and kinetic models.

$$R^2 = \frac{\sum (q_{mean} - q_{cal})^2}{\sum (q_{cal} - q_{mean})^2 + \sum (q_{cal} - q_{exp})^2} \tag{3}$$

$$\chi^2 = \sum \frac{(q_{exp} - q_{cal})^2}{q_{cal}} \tag{4}$$

3. Results and discussion

3.1. Phytochemical study of Psidium guajava

The PG extracts were subjected to qualitative and quantitative phytochemical screening as shown by the results presented in Table 1. According to the results, the phytochemical analysis indicates that crude PG-extracts contain biomolecules such as alkaloids, phenols, tannins, flavonoids, terpenoids and glucosides. Carbohydrates, phytosterol and steroids were not present in the PG extract (Table 1). A higher composition of phenols (90.16 ± 0.03) was identified, followed by saponins (90.16 ± 0.03), flavonoids (28.55 ± 0.03), alkaloids (25.48 ± 0.01), tannins (16.22 ± 0.02) and terpenoids (5.40 ± 0.02). Phytoconstituents found in biomolecules such as alkaloids, phenols, flavonoids, saponins, tannins, and terpenoids found in *Psidium guajava* leaves extracts work as reducing and stabilizing agents. Plant leaf extract plays a significant part in metal and metal oxide synthesis because it contains a variety of phytochemicals which are important for initiating, accelerating, and completing the green synthesis of nanoparticles. Similar functions had earlier been reported in the literature on the phytochemicals of plant extracts (Doan et al., 2020; Fernández et al., 2020; Karpagavinayagam et al., 2020).

3.2. Characterizations of PG-NiONPs

3.2.1. Crystalline structure analysis

The crystalline structure and phase characteristics of PG-NiONPs nanoadsorbents were examined by X-ray diffraction (XRD) technique and shown in Fig..2a. The results of the experimental diffractogram of PG-NiONPs were matched with the database of XRD. According to Fig..2a, the characteristic diffraction peaks were identified at the 2 Theta of 37.26°, 43.26°, 62.93°, 75.63° and 79.74° which were assigned to the crystal planes (111), (200), (220), (311) and (222).

Overall, the PG-NiONPs indicated face-centred cubic (FCC) crystalline structure of nickel oxide (Bunsenite) nanoparticles(JCPDS Card no. 047–1049) (Ezhilarasi et al., 2020; Gebretinsae et al., 2019). It is evident from the characteristic peaks of the XRD patterns that impurities such as $Ni(OH)_2$ were detected, thereby indicating the formation of pure monophasic nickel oxide nanoparticles. Particularly, the Debye-Scherrer

Table 1
Phytochemical analysis of *Psidium guajava* leaves extract.

Phytochemical	Qualitative	Quantitative (mg/g)
Alkaloids	++	25.48 ± 0.01
Phenols	+++	90.16 ± 0.03
Carbohydrates	–	Nd
Tannins	++	16.22 ± 0.02
Phytosterol	–	Nd
Flavonoids	+++	28.55 ± 0.03
Saponins	+++	30.62 ± 0.01
Terpenoids	+	5.40 ± 0.02
Steroids	–	Nd
Glucosides	+	2.42 ± 0.04

Key: Present = +; Absent = -; Nd = Not determined.

equation shown in Eq. (S2) was applied to evaluate the average crystallite of the PG-NiONPs (Lingaraju et al., 2020). The result revealed that the average crystallite size of 21.20 nm was confirmed, indicating the nanoscale dimensions of the nickel oxide nanoparticles.

3.2.2. Functional group analysis

The functional group spectrum present on the PG-NiONPs was conducted using FTIR Spectroscopy to validate the nature and purity of the nanoparticles as shown in Fig. 2b. The results indicate the occurrence of absorption peaks within the range of 400 to 4000 cm^{-1}. Overall, the FTIR peaks were detected at 470, 1092, 1600, 3172 and 3668 cm^{-1}, respectively, indicating the vibrational modes in the produced nanoparticles. Correspondingly, the peak occurrence at 470 cm^{-1} was assigned to the stretching vibration of Ni-O, which indicate the nanoscale range of the width of crystals of bunsenite nickel oxide nanoparticles phase (Fernández et al., 2020; Ghazal et al., 2020). The broad absorption peak at 1092 cm^{-1} showed correspondence to the stretching vibration of C-O bonds due to the presence of the phenolic groups from the PG extract and the precursor salt (Goel et al., 2020). Particularly, the peak occurrence at 1600 cm^{-1} may be attributed to the C = O stretching and H-O-H bending that is associated with the carbonyl groups and chloride ions absorption from water in the air during the calcination process (Ghazal et al., 2020). The vibration band identified at 3172 cm^{-1} was linked to the O-H stretching of the carboxyl groups. Similarly, the FTIR peak at 3668 cm^{-1} corresponds to the stretching vibrations of O-H attributed to the hydroxyl groups due to the presence of water molecules (Fernández et al., 2020; Goel et al., 2020).

3.2.3. Morphological analysis

The structural morphology of PG-NiONPs was conducted using HRSEM and the result is shown in Fig. 2c. As can be seen from the result, a cylindrical and rod-like surface shape was obtained. The obtained morphology may be influenced by numerous parameters such as solvent preference, capping agents, and experimental conditions of temperature and time, which may be related to the reaction mechanism (Fernández et al., 2020). The self-aggregation of nickel oxide nanoparticles may be due to the collective behaviour of electrostatic interactions and Vander Waals forces (Zahra and Ahmad, 2020). The form and size of the nickel oxide nanoparticles may be impacted by the nature of the extract and the concentration of the capping agents (Ezhilarasi et al., 2020; Goel et al., 2020). Therefore, the green synthesis approach and the utilized PG extract favoured the successful synthesis of nickel oxide nanoparticles with a rod-like and cylindrical architecture. The morphological representation of the PG-NiONPs revealed an average particle size of 20.96 nm which aligned in the nanoscale range. Notably, the result of PG-NiONPs particle size obtained from the HRSEM showed agreement with the XRD analysis in Fig. 2a. Furthermore, elemental distributions present in the produced PG-NiONPs were established using energy

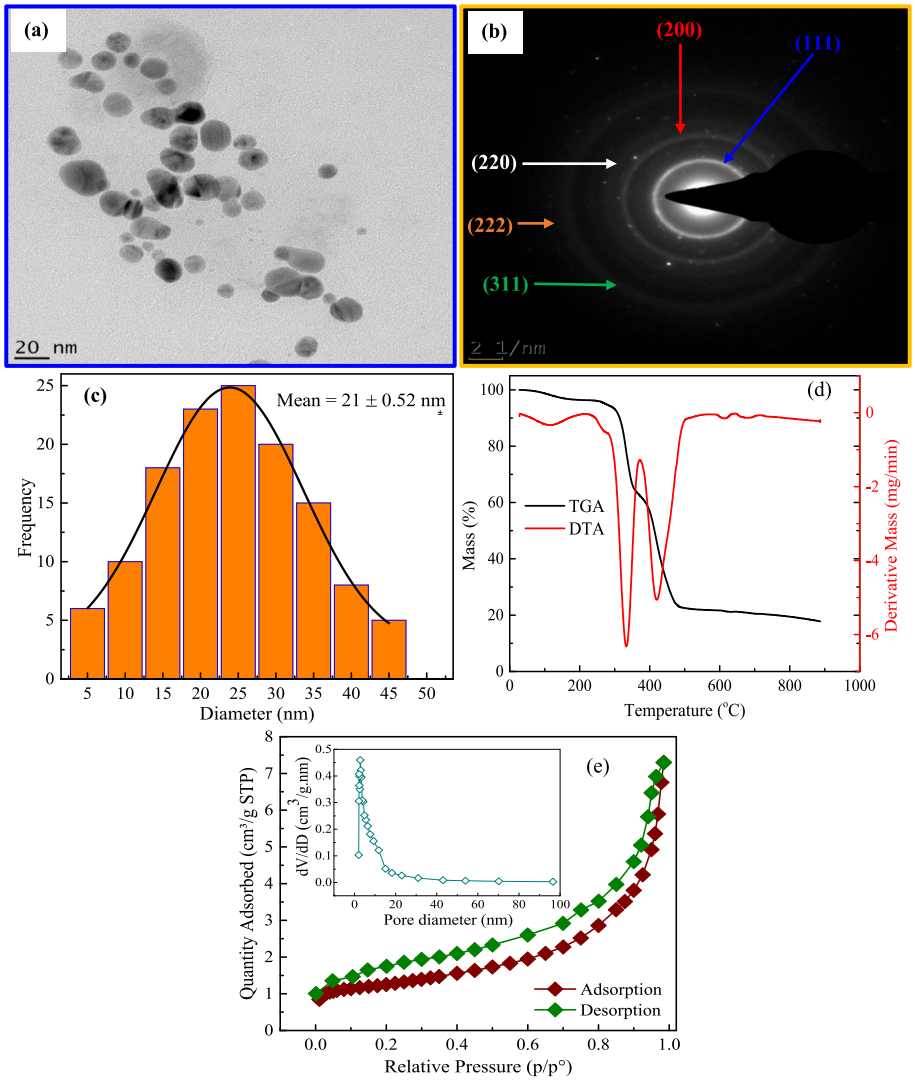

Fig. 2. (a) XRD of PG-NiONPs; (b) FTIR of PG-NiONPs; (c) HRSEM of PG-NiONPs and (d) EDX analysis of PG-NiONPs.

dispersive X-ray spectrometer (EDX) analysis as shown in Fig. 2d. Overall, the EDX result showed the elemental compositions of Ni (55.57%), O (33.41%), C (10.50%) and K (0.52%). Hence, the appearance of Ni and O was predominant, followed by C and K. The EDX result of the elemental analysis confirmed the fabrication of smooth, layered, aggregated and irregularly dispersed nickel oxide nanoparticles. In all, particle sizes of 16 and 23.21 nm were reported by Ghazal et al. and Karpagavinayagam et al. for nickel oxide nanoparticles (Ghazal et al., 2020; Karpagavinayagam et al., 2020).

3.2.4. Microstructural analysis

The produced nanoparticles powder was slightly agglomerated with a degree of sharp edges, as seen in a typical HRTEM image of PG-NiONPs in Fig. 3a. Surprisingly, the SAED pattern of PG-NiONPs displayed in Fig. 3b exhibited multiple strongly defined diffraction rings attributed to the distinct crystallographic planes of (111), (200), (220), (311), and (312). (222).

This observation was verified by the XRD data, which showed that the generated PG-NiONPs had a high degree of polycrystallinity. In Fig. 3c, the results of the particle size distribution of PG-NiONPs are shown, with an average mean particle size of 21 ± 0.52.

3.2.5. Thermal stability tests

Thermogravimetric analysis (TGA) and derivative mass (DTA) loss were used to determine the thermal stability of PG-NiONPs, as shown in Fig. 3d.

The given results showed that mass loss happened in three stages in the temperature ranges of 50 to 300 °C, 300 to 352 °C, and 352 to 485 °C. The first 2.29% weight loss happened quickly between 50 and 300 °C, with a concentrated endothermic peak at 100 °C that corresponds to the volatilization of water (Du et al., 2022b). Weight loss of 28.06% was found between the temperatures of 300 and 352 °C, with a centred endothermic peak at 334 °C. The thermal disintegration of Ni $(OH)_2$ in line with $Ni(OH)_2 \rightarrow NiO + H_2O$ was attributed to the weight loss at this temperature zone (Fernández et al., 2020). At the centred endothermic peak of 441 °C during the last decomposition stage (352 to 485 °C), a mass decomposition of 43.51% was observed. The identified loss in mass may be attributed to the decomposition of different oxygen-containing groups on the surface of nickel oxide nanoparticles (Du et al., 2022b; Fernández et al., 2020). Besides, mild weight loss in the range of 485–900 °C might be related to the degradation of more stable functional groups of samples.

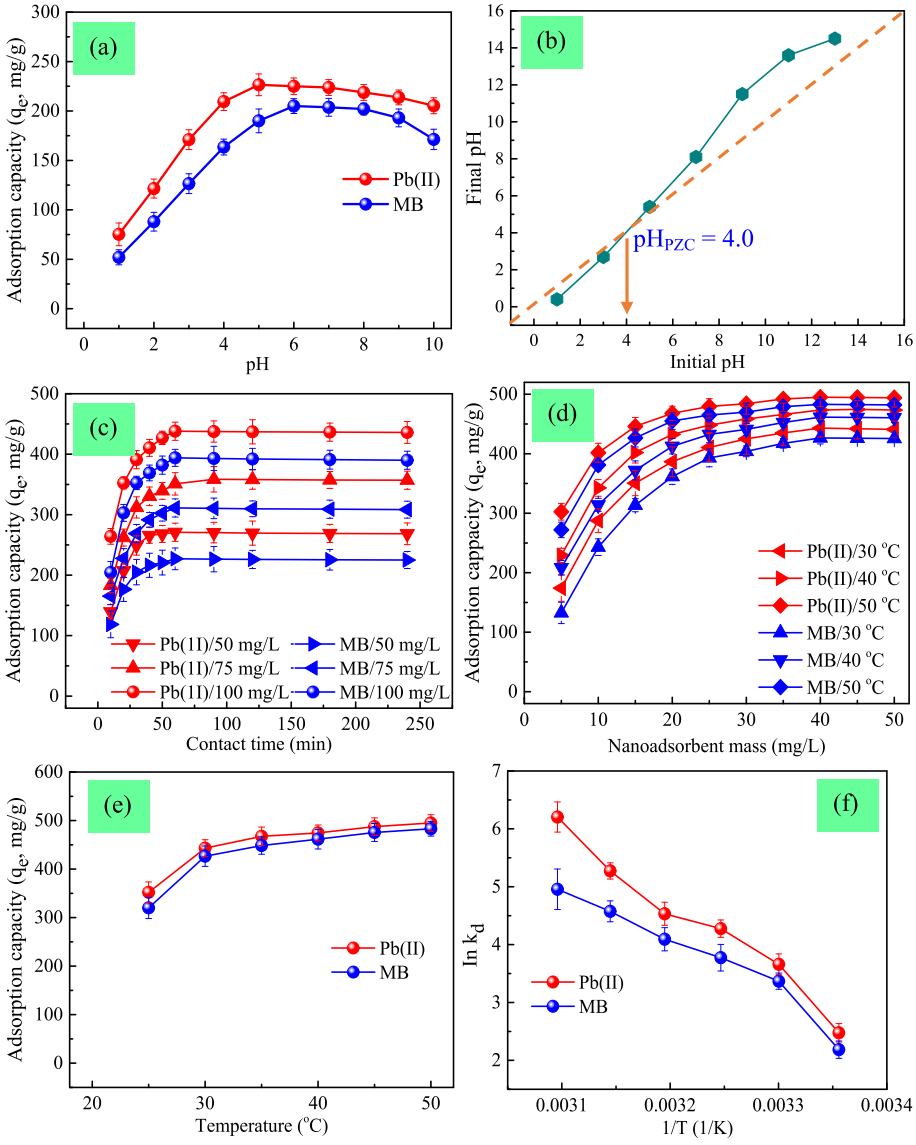

Fig. 3. (a) HRTEM image of PG-NiONPs; (b) SAED image of PG-NiONPs; (c) particle size distribution of PG-NiONPs; (d) TGA of PG-NiONPs and (e) N_2 adsorption–desorption isotherms of PG-NiONPs with the pore size distribution.

3.2.6. Surface properties

The N_2 adsorption approach was used to get the specific surface areas (BET), pore volume, and pore size of PG-NiONPs to better understand their surface architecture. In Fig. 3e, the nitrogen adsorption–desorption isotherms of PG-NiONPs suggested a type IV isotherm. The hysteresis loop was also visible without parallel representation at intermediate high pressure, which corresponded to the mesoporous structure of PG-NiONPs. The two branches of the nickel oxide nanoparticles' hysteresis loop were separated, indicating efficient surface qualities appropriate for adsorption experiments. PG-NiONPs had a surface area of 85.40 m^2/g, a pore volume of 0.37 cm^3/g, and a pore size of 18 nm, respectively. By improving the removal of dyes and heavy metals contaminated wastewater, the surface characteristics of nanoparticles give information on the availability of interfacial area and binding sites for the occurrence of nanoadsorbent-adsorbate interaction (Bhaumik et al., 2021). Importantly too, the obtained pore size for PG-NiONPs is in the range of 2 to 50 nm, indicating that the prepared nanoparticles are mesoporous. Overall, the XRD, FTIR, HRSEM, and HRTEM results corroborated the surface properties characterization results of the PG-NiONPs, indicating successful green synthesis of nickel oxide nanoparticles using PG-extract.

3.3. Adsorption studies

In this adsorption study, the adsorption performance of MB and Pb (II) ions was systematically conducted using PG-NiONPs. The batch experiments examined the influence of various parameters such as; solution pH, contact time, nanoadsorbent mass and temperature on the removal of MB molecules and Pb(II) ions by PG-NiONPs in a conical flask using the working volume of 100 mL. The data from these experiments were utilized for the kinetics, isotherm and thermodynamics analysis.

3.3.1. Impact of solution pH

Overall, pH is a key adsorption parameter influencing the removal of dyes and heavy metals by introducing change in the nanoadsorbents surface charge, ionization degree of functional groups and adsorbate speciation (Egbosiuba and Abdulkareem, 2021). Under various pH conditions, PG-NiONPs exhibited different MB and Pb(II) adsorption capacities, indicating that the existence of the adsorbates in aqueous solutions shows a close relation to pH values. As displayed by the solution pH results shown in Fig. 4a, the adsorption capacity of MB by PG-NiONPs increased from 52.40 to 205.22 mg/g in the pH range of 1 to 6. Further increment in the pH beyond 6 progressively declined the adsorption capacity to 171.20 mg/g at pH 10. On the other hand, Pb(II) adsorption capacity increased from 75.25 to 226.45 mg/g at the pH range of 1 to 5. Beyond the pH of 5, the adsorption capacity of Pb(II) decreased significantly to 205.25 mg/g at a pH of 10. The trend of the observed results of MB and Pb(II) adsorption at lower pH values may be linked to the competition for the active sites of adsorption between the adsorbates and the protons (H^+) (Yimin et al., 2018). However, as the pH increases, the formation of hydroxide (OH^-) ion enhances electrostatic attraction between the adsorbates and the nanoadsorbent.

The determination of the pH point of zero charges (pH_{PZC}) was conducted to explore the reason for the variation of adsorption capacity with pH using the method reported elsewhere with a little modification (Mustapha et al., 2022) and the result shown in Fig. 4b. Accordingly, the corresponding pH_{PZC} was obtained as 4.0, indicating that PG-NiONPs is positively charged at pH lower than 4.0 and negatively charged at pH higher than 4.0. Thus, the positive surface charge of the PG-NiONPs at low values of the pH inhibits the uptake of MB and Pb(II) due to

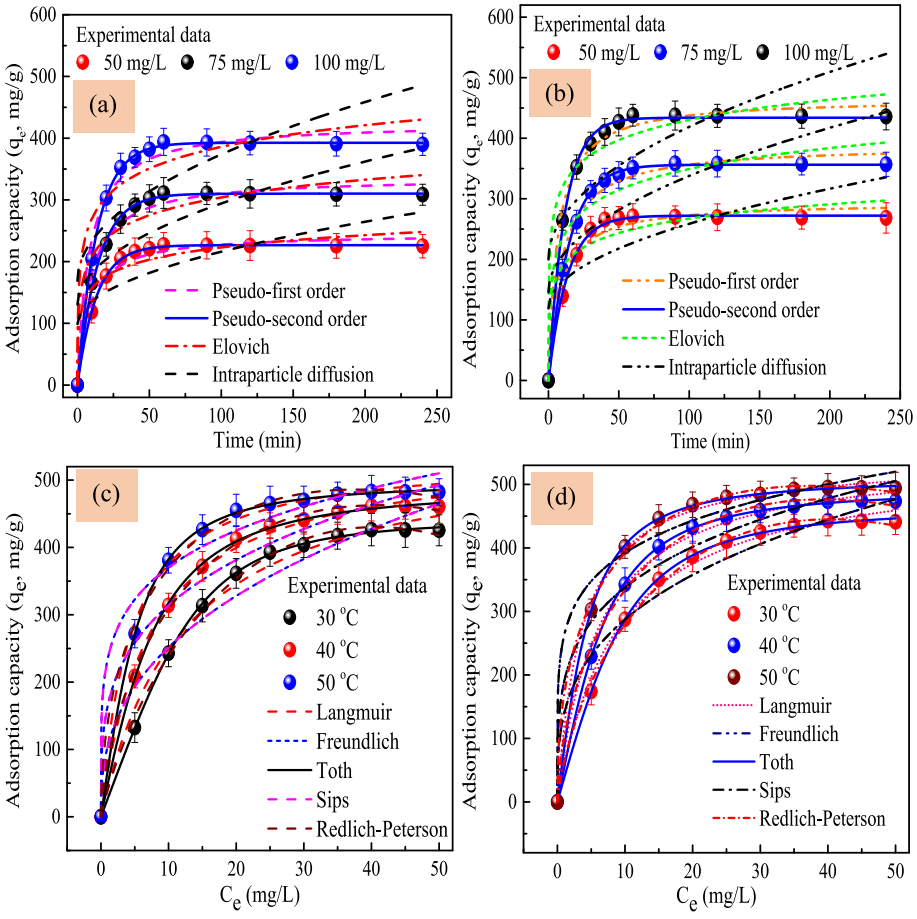

Fig. 4. (a) Effects of solution pH on the removal of MB and Pb(II) at initial concentration (50 mg/L), contact time (20 min), nanoadsorbent mass (20 mg/L) and temperature (30 °C); (b) pH_{PZC} determination of PG-NiONPs; (c) effects of contact time on the MB and Pb(II) adsorption by PG-NiONPs at different initial concentrations (50, 75 and 100 mg/L), pH (6 for MB and 5 for Pb(II), nanoadsorbent mass (20 mg/L) and temperature (30 °C); (d) effects of nanoadsorbent mass ((pH = MB(6) and Pb(II)(5), contact time = 60 min, initial MB/Pb(II) concentration = 100 mg/L and temperature = 30 °C); (e) effects temperature ((pH = MB(6) and Pb(II)(5), contact time = 60 min, initial MB/Pb(II) concentration = 100 mg/L and nanoadsorbent mass = 40 mg/L) on the removal of MB and Pb(II) by PG-NiONPs and (f) the plot of $\ln(K_c)$ vs 1/T.

protonation leading to electrostatic repulsion between the positively charged nanoadsorbent and the adsorbate (Uko et al., 2022). However, at a higher pH value above 4.0, the adsorption of MB and Pb(II) increased significantly due to the deprotonation of functional surface groups (Wang et al., 2022a). As such, higher adsorption of MB and Pb(II) may be attributed to the electrostatic attraction between the negatively charged surface of PG-NiONPs and the positively charged adsorbates. The observed adsorption capacities of 171.20 and 205.25 mg/g for MB and Pb(II) at pH of 10 indicate that electrostatic attraction is not the only adsorption mechanism, but others such as pore filling, hydrogen bonding and π-π interaction may also be responsible. In the current study, further MB and Pb(II) adsorption experiments were performed at optimal pH values of 6 and 5 were used.

3.3.2. Impact of contact time

At varying MB and Pb(II) concentrations of 50, 75, and 100 mg/L, the influence of contact duration on the adsorption capacity of MB and Pb(II) by PG-NiONPs was investigated from 5 to 300 min. The results shown in Fig. 4c indicate that the MB and Pb(II) adsorption increased quickly during the first 30 min, then gradually increased until 60 min when equilibrium was reached. Particularly, the adsorption capacity of PG-NiONPs for MB increased from 118.50 to 227.50 mg/g, 165.20 to 311.15 mg/g and 204.50 to 394.00 mg/g at the initial dyes concentrations of 50, 75 and 100 mg/L. On the other hand, the adsorption of Pb(II) ion onto the PG-NiONPs at the initial metal ion concentrations of 50, 75 and 100 mg/L further increased from 139.43 to 270.88 mg/g, 183.00 to 358.50 mg/g and 264.15 to 438.00 mg/g, respectively. The observed increase in the adsorption capacities of MB and Pb(II) may be ascribed to the surface area of PG-NiONPs, increased diffusion of MB/Pb(II) and the binding sites accessibility of the MB and Pb(II) (Yan et al., 2022). Remarkably, there was no noticeable increase in the adsorption capacity of the MB/Pb(II) with a further increase in contact time up to 240 min. This may be linked to the possible occupation and saturation of adsorption sites on the PG-NiONPs surface (Egbosiuba, 2022b). Particularly at each contact time, the adsorption capacity of the adsorbates by the nanoadsorbent increased as the concentration of the MB/Pb(II) solutions of 50, 75 and 100 mg/L. The equilibrium time was obtained as 60 min and was used to carry out further adsorption experiments, while the concentration of the adsorbates was regulated at 100 mg/L.

3.3.3. Impact of nanoadsorbent mass

In consideration of the treatment effectiveness of MB and Pb(II) by PG-NiONPs, nanoadsorbent mass is a major factor that needs to be optimized. For this purpose, the effect of nanoadsorbent mass on the adsorption capacity of MB and Pb(II) was explored in the range of 5 to 50 mg/L at different temperatures of 30, 40 and 50 °C, respectively. The results presented in Fig. 4d revealed that increasing the dose of PG-NiONPs from 5 to 40 mg/L enhanced the adsorption capacity of MB from 132.50 to 426.50 mg/g, 208.30 to 461.62 mg/g and 272.22 to 483.64 mg/g at the temperatures of 30, 40 and 50 °C, respectively. On the other hand, the adsorption capacity of Pb(II) at the temperatures of 30, 40 and 50 °C improved visibly from 174.31 to 443.05 mg/g, 229.25 to 473.50 mg/g and 302.10 to 495.22 mg/g using PG-NiONPs mass of 5 to 40 mg/L. At 50 °C in this work, MB and Pb(II) removal efficiencies were 96.50% and 99.00%, respectively. The availability of a significant number of adsorption sites may be related to the efficiency of PG-NiONPs in the removal of MB and Pb(II) (Tran et al., 2022; Yan et al., 2022). However, it was found that the MB and Pb(II) solutions' adsorption capacity remained constant beyond a concentration of 40 mg/L, indicating that the concentration gradient between the nanoparticles and MB/Pb(II) solutions was split as effectively as possible (Aragaw and Alene, 2022). This may also be due to the saturation of the adsorption limit brought on by increasing the mass of the nanoadsorbent, which results in an inverse relationship between the adsorption capacity per gram and the nanoadsorbent mass at a fixed adsorbate concentration (Yadav and Dasgupta, 2022). Pb(II) ion displayed higher adsorption capacity values than MB at a different mass of the nanoadsorbent and temperatures, which might be related to the ion's divalent nature and electronegative characteristics (Sellaoui et al., 2019). The adsorption studies that followed employed the ideal nanoadsorbent mass of 40 mg/L.

3.3.4. Impact of temperature

To explore the effect of temperature on the adsorption phenomenon of MB and Pb(II) by PG-NiONPs, the study was carried out in the temperature range of 25 to 50 °C and the results are displayed in Fig. 4e. As can be seen from the results, the adsorption capacity of the MB and Pb (II) manifested a significant increment with temperature increase. Typically, the adsorption capacity of MB increased from 320.13 to 483.50 mg/g, while that of Pb(II) increased from 352.05 to 495.40 mg/g in the temperature range of 25 to 50 °C. In general, this may be ascribed to the increment in the speed of MB/Pb(II) movement in solution as the temperature increases, thereby enhancing the diffusion of the adsorbates on the nanoadsorbent charged surface due to the availability of abundant energy (Hashemzadeh et al., 2022). In all, the adsorption process in this study is more effective at elevated temperatures.

3.3.5. Adsorption kinetics

The study of the adsorption kinetics is important to understand the adsorption rate and the prediction of the cost-effective adsorption mechanism of wastewater treatment design. For the adsorption of MB and Pb(II) by PG-NiONPs, the experimental data were fitted to the pseudo-first-order (Eq. (5)), pseudo-second-order (Eq. (6)), Elovich (Eq. (7)) and intraparticle diffusion (Eq. (8)) models (Abdulkareem et al., 2023; Aliyu et al., 2023; Gómez-Avilés et al., 2022; Jain et al., 2022) for the kinetic data analysis.

$$q_t = q_e\left(1 - e^{-k_1 t}\right) \tag{5}$$

$$q_t = \frac{k_2 q_e^2 t}{1 + k_2 q_e t} \tag{6}$$

$$q_t = \frac{1}{\beta}\ln(1 + \alpha\beta t) \tag{7}$$

$$q_t = k_{ID} t^{\frac{1}{2}} + C \tag{8}$$

where q t and q e (mg/g) represent the amounts of MB and Pb(II) ions adsorbed at equilibrium over a set length of time. The constant rates for pseudo-first order, pseudo-second order, initial adsorption rate, and intraparticle diffusion are denoted by the symbols k_1 (1/min), k_2 (mg/g min), α (g mg^{-1} min^{-2}) and k_{ID}, respectively. The values, β (mg g^{-1} min^{-1}) and C (mg/g) represent the intercept and surface coverage degree related to the activation energy of chemisorption.

The kinetic data for the adsorption of MB and Pb(II) on PG-NiONPs were fitted to the pseudo-first order, pseudo-second order, Elovich and intraparticle diffusion models for the understanding of the reaction dynamics of MB/Pb(II) adsorption and the adsorption rate definition at the initial MB and Pb(II) concentrations of 50, 75 and 100 mg/L as shown in Fig. 5(a,b), while Table 2 specifically presents the evaluated kinetic parameters and the correlation coefficients. The pseudo-second-order kinetic model fitted the adsorption data of PG-NiONPs for MB and Pb(II) adsorption better, indicating that the adsorption process is chemisorption controlled and the adsorption rate defined by the number of binding sites on the surface of the nanoadsorbent (Jain et al., 2022; Wang et al., 2022a; Wang et al., 2022b). Furthermore, the theoretical adsorption capacities of PG-NiONPs for MB and Pb(II) adsorption approached the actual adsorption capacities, thereby further validating that the behaviour of the adsorption process was best represented by the pseudo-second-order kinetic model. Correspondingly, the pseudo-second-order kinetic model presented the highest correlation coefficient (R^2) close to unity and the lowest error values evaluated using the

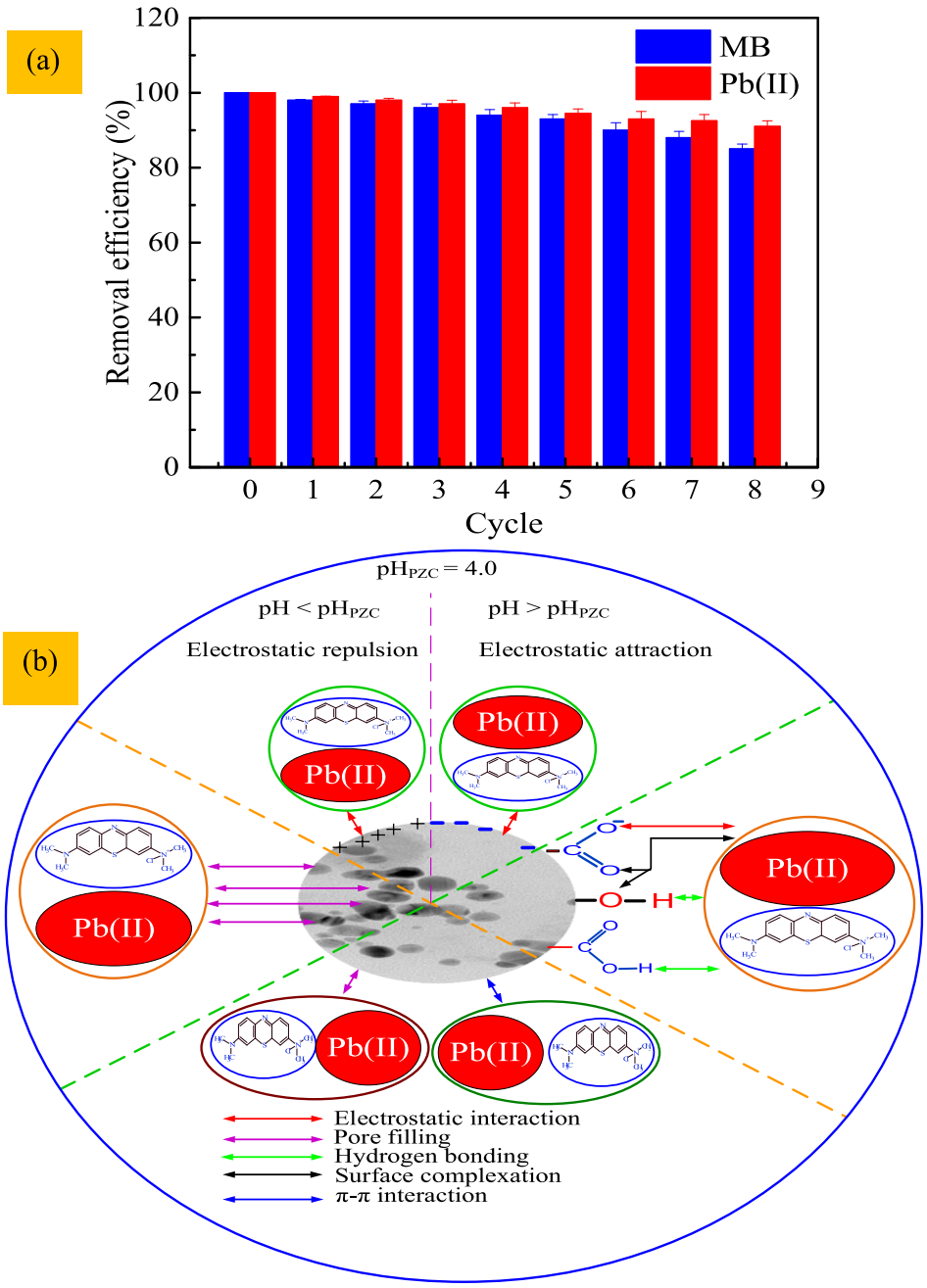

Fig. 5. Kinetic data fitting of (a) MB and (b) Pb(II) at different initial concentrations to pseudo-first order, pseudo-second order, Elovich and intra-particle diffusion kinetic models at the pH (6 and 5 for MB and Pb(II)), contact time (60 min), nanoadsorbent mass (40 mg/L) and temperature (30 °C); Fitting of isotherm data of (c) MB and (d) Pb(II) at different temperatures to the Langmuir, Freundlich, Toth, Sips and Redlich-Peterson isotherm models (pH = 6 and 5 for MB and Pb (II), contact time = 60 min, nanoadsorbent mass = 40 mg/L and temperature = 30 °C).

X^2 and SSE, respectively as shown in Table 2. The adsorption fitness trend of the experimental data to the kinetic model followed the order; pseudo-second order > pseudo-first order > Elovich > intraparticle diffusion models.

More significantly, the k_1 and k_2 values decreased as the starting concentrations of MB and Pb(II) increased from 50 to 100 mg/L, showing that chemisorption was not the only rate-limiting factor and that both physisorption and chemisorption were responsible for controlling the adsorption process. For the Elovich model, the parameter 1/β suggests the available number of active sites for the adsorption of MB and Pb(II) from wastewater. Observably from Table 2, the available active sites increased with the elevation in adsorbate concentration. Generally, the solid–liquid adsorption process involves three basic stages (i) adsorbate transport from the bulk solution to the nano-adsorbent surface, (ii) intraparticle diffusion for porous media and (iii) film (boundary layer) diffusion for nonporous media due to the external mass transport (Jain et al., 2022; Wang et al., 2022a; Wang et al., 2022b). The results on the intraparticle diffusion revealed a significant correlation coefficient and a non-zero intercept value, thus indicating that this model may not suitably define the kinetics and rate-controlling mechanism of MB and Pb(II) adsorption by PG-NiONPs. Noticeably, the demonstration of the multi-linear plots of the kinetic data suggests that the external mass transport of boundary layer diffusion influenced the early stages of the adsorption process, while the later progressive adsorption stage was dominated by an intraparticle diffusion process.

3.3.6. *Adsorption isotherm*

Adsorption isotherms provide important information relating to the surface properties of the nanoadsorbent, the adsorption mechanisms and the nanoadsorbent-adsorbate interaction. The MB and Pb(II) adsorption isotherms on PG-NiONPs were investigated at temperatures of 30, 40 and 50 °C, respectively. In addition to the two-parameter models,

Table 2
Estimated kinetic model parameters of MB and Pb(II) ion adsorption using PG-NiONPs.

Kinetic model	Parameters	Adsorbate MB Initial dye concentration (mg/L)			Pb(II) Initial metal ion concentration (mg/L)		
		50	75	100	50	75	100
	$q_{e,\ exp}$ (mg/g)	227.88 ± 0.06	311.50 ± 0.07	394.47 ± 0.05	271.15 ± 0.08	351.24 ± 0.04	438.10 ± 0.10
Pseudo-first order	$q_{e,\ cal}$ (mg/g)	245.43 ± 0.09	336.73 ± 0.08	425.67 ± 0.09	294.44 ± 0.05	388.69 ± 0.06	466.01 ± 0.09
	$K_1 \times 10^{-4}$ (1/min)	5.15 ± 0.02	3.47 ± 0.02	2.89 ± 0.01	4.28 ± 0.02	2.84 ± 0.01	3.31 ± 0.03
	X^2	115.54	170.20	318.25	232.441	180.16	170.66
	SSE	1039.89	1531.78	2864.24	2091.97	1621.47	1535.93
	R^2	0.977	0.982	0.979	0.968	0.985	0.990
Pseudo-second order	q_e (mg/g)	226.67 ± 0.03	310.11 ± 0.04	392.57 ± 0.08	272.12 ± 0.06	356.34 ± 0.07	433.96 ± 0.08
	K_2 (g mg^{-1} min^{-1})	0.08 ± 0.02	0.07 ± 0.01	0.07 ± 0.03	0.08 ± 0.03	0.07 ± 0.02	0.09 ± 0.01
	X^2	2.15	18.35	7.26	17.61	11.76	52.42
	SSE	19.36	165.19	65.32	158.50	105.88	471.80
	R^2	0.999	0.998	0.999	0.998	0.999	0.997
Elovich	α (g mg^{-1} min^{-2})	691.70 ± 0.08	640.64 ± 0.10	1033.58 ± 0.13	844.65 ± 0.12	547.64 ± 0.09	3695.16 ± 0.11
	β (mg g^{-1} min^{-1})	0.04 ± 0.01	0.02 ± 0.01	0.02 ± 0.01	0.03 ± 0.01	0.02 ± 0.01	0.02 ± 0.01
	1/ β	28.57 ± 0.02	41.60 ± 0.04	52.63 ± 0.07	34.48 ± 0.04	50.00 ± 0.05	66.60 ± 0.08
	X^2	398.42	655.98	1152.14	681.47	806.55	880.00
	SSE	3585.82	5903.84	10369.29	6133.22	7258.93	7920.00
	R^2	0.919	0.929	0.923	0.906	0.934	0.950
Intraparticle diffusion	K_{ID} (mg/g.$min^{0.5}$	11.73 ± 0.01	16.39 ± 0.02	20.47 ± 0.04	13.98 ± 0.02	19.20 ± 0.03	21.90 ± 0.02
	C (mg/g)	98.77 ± 0.02	130.43 ± 0.05	169.03 ± 0.08	119.02 ± 0.07	145.76 ± 0.08	199.96 ± 0.09
	X^2	2393.69	4184.85	7028.98	3594.84	5275.15	8661.73
	SSE	21543.24	37663.65	63260.83	32353.57	47476.38	77955.55
	R^2	0.518	0.548	0.528	0.503	0.571	0.508

Langmuir (Eq. (9)) (Egbosiuba et al., 2021b) and Freundlich (Eq. (10)) (Tran et al., 2022) that are most frequently employed, several three-parameter isotherms (Toth, (Eq. (11) (Gómez-Avilés et al., 2022), Sips (Eq. (12) (Zhang et al., 2022) and Redlich-Peterson (Eq. (13) (Wang et al., 2022a; Wang et al., 2022b)) were examined to explore the mechanism and interaction between the nanoadsorbent and the adsorbate using the following mathematical representations.

$$q_e = \frac{q_m b C_e}{1 + K_L C_e} \tag{9}$$

$$q_e = K_F C_e^{1/n} \tag{10}$$

$$q_e = \frac{q_m K_t C_e}{(1 + (K_t C_e)^n)^{\frac{1}{n}}} \tag{11}$$

Table 3
Evaluated isotherm model parameters for MB and Pb(II) ion adsorption onto PG-NiONPs.

Isotherm model	Parameters	Adsorbate MB Temperature (°C)			Pb(II)		
		30	40	50	30	40	50
	$q_{m,\ exp}$ (mg/g)	426.42 ± 0.04	461.31 ± 0.03	483.03 ± 0.06	443.43 ± 0.08	473.22 ± 0.06	495.64 ± 0.08
	q_m (mg/g)	557.22 ± 0.05	543.51 ± 0.04	537.24 ± 0.03	539.09 ± 0.05	546.54 ± 0.04	541.48 ± 0.09
	K_L (L/min)	0.08 ± 0.01	0.14 ± 0.02	0.23 ± 0.01	0.11 ± 0.03	0.17 ± 0.01	0.28 ± 0.03
Langmuir	R_L	0.12 ± 0.02	0.06 ± 0.01	0.03 ± 0.02	0.79 ± 0.01	0.44 ± 0.03	0.21 ± 0.02
	X^2	253.23	87.53	91.88	146.55	110.06	60.79
	SSE	2279.08	787.78	826.93	1318.92	990.53	547.13
	R^2	0.987	0.996	0.996	0.993	0.995	0.997
	K_F (mg/g)	104.54 ± 0.03	164.62 ± 0.05	234.28 ± 0.01	139.19 ± 0.03	189.76 ± 0.01	262.20 ± 0.05
	n_F	2.62 ± 0.02	3.57 ± 0.04	5.03 ± 0.03	3.18 ± 0.02	4.00 ± 0.04	5.72 ± 0.02
Freundlich	X^2	1017.66	688.24	647.43	834.37	763.12	528.34
	SSE	9158.89	6194.17	5826.87	7509.30	6868.12	4755.14
	R^2	0.949	0.967	0.970	0.958	0.965	0.976
	q_m (mg/g)	441.01 ± 0.07	487.44 ± 0.09	495.58 ± 0.05	462.25 ± 0.06	491.20 ± 0.05	508.56 ± 0.08
	k_t (L/mg)	0.06 ± 0.02	0.10 ± 0.03	0.14 ± 0.01	0.08 ± 0.02	0.11 ± 0.03	0.17 ± 0.02
Toth	n	1.26 ± 0.03	1.10 ± 0.01	1.09 ± 0.04	1.09 ± 0.01	1.05 ± 0.02	1.02 ± 0.01
	X^2	8.98	14.52	5.62	8.25	4.03	5.03
	SSE	71.84	116.18	44.93	65.99	32.21	40.27
	R^2	0.999	0.999	0.999	0.999	0.999	0.999
	q_m (mg/g)	78.11 ± 0.03	152.01 ± 0.07	233.09 ± 0.08	150.67 ± 0.06	255.19 ± 0.08	215.36 ± 0.09
	k_s (L/mg)	26.43 ± 0.02	12.60 ± 0.03	1.20 ± 0.03	−11.48 ± 0.01	−65.43 ± 0.02	46.85 ± 0.03
Sips	m	0.98 ± 0.01	0.98 ± 0.02	0.92 ± 0.01	0.92 ± 0.02	0.95 ± 0.01	0.98 ± 0.02
	X^2	1144.86	774.27	728.36	938.66	858.51	594.39
	SSE	9158.89	6194.17	5826.87	7509.30	6868.12	4755.14
	R^2	0.943	0.963	0.966	0.953	0.960	0.973
	K_{RP} (L/mg)	−77.62 ± 0.05	−29.70 ± 0.03	−13.81 ± 0.01	−72.84 ± 0.02	–23.02 ± 0.01	−10.54 ± 0.01
	α	37.33 ± 0.01	114.39 ± 0.07	154.16 ± 0.09	136.45 ± 0.05	124.82 ± 0.04	179.34 ± 0.08
Redlich-Peterson	β	0.95 ± 0.02	0.92 ± 0.01	0.92 ± 0.01	0.99 ± 0.01	0.95 ± 0.01	0.94 ± 0.01
	X^2	72.51	44.13	81.805	61.849	84.114	57.660
	SSE	580.07	353.03	654.439	494.792	672.912	461.280
	R^2	0.996	0.998	0.996	0.997	0.996	0.997

$$q_e = \frac{q_m(K_sC_e)^m}{1+(K_sC_e)^m} \quad (12)$$

$$q_e = \frac{K_RC_e}{1+a_RC_e^{\beta}} \quad (13)$$

where q_e and q_m, both expressed in mg/g, stand for the amount of MB and Pb(II) ions removed at equilibrium and the maximum adsorption capacity for the monolayer distribution on the surface of PG-NiONPs, respectively. Overall, the concentration of MB/Pb(II) at equilibrium, the Langmuir adsorption constant at equilibrium, the separation factor, the Freundlich adsorption constant, and the Freundlich parameter associated with heterogeneity (n1) are represented by C_e (mg/L), K_L (L/mg), R_L, K_F and n. Additionally, K_t (L/mg), K_s (L/mg), K_{RP} (L/mg) stand for the isotherm model constants for the Toth, Sips, and Redlich-Peterson, respectively, while n, m, α and β stand for the exponents for the Toth, Sips, and Redlich-Peterson, respectively.

Fig. 5(c,d) shows how the experimental data from the isotherm adsorption experiments were fitted to the isotherm models, and Table 3 contains the evaluated isotherm parameters, correlation coefficient (R^2) and error values. Toth isotherm model fits the experimental data better than Langmuir, Freundlich, Sips, and Redlich-Peterson isotherm models for both MB and Pb(II) adsorption, as shown by the results. Remarkably in Table 3, the Toth isotherm model had the lowest values for the X^2 and SSE while also having R^2 values that were closer to unity than those of the other four models for both MB and Pb(II) adsorption by PG-NiONPs. As a result, the Redlich-Peterson, Langmuir, Freundlich, and Sips isotherm models were shown to be less consistent with the MB and Pb(II) adsorption process than the Toth isotherm model. Table 3 shows the maximum adsorption capacity obtained from the Toth isotherm model as 495.58 and 508.56 mg/g for MB and Pb(II). As shown in Table 4, the adsorption capacity of PG-NiONPs was higher compared to the adsorption capacity of other nanoadsorbents reported in the literature.

For the Langmuir isotherm model, the isotherm constant (K_L) shows proportionality to the pore volume and surface area, thereby indicating that an increment in the surface properties results in the enhancement of the adsorption capacity (Wang et al., 2022a; Wang et al., 2022b). The determined separation factor (R_L) was in the range of zero to one for both adsorbates, indicating that the adsorption was a favourable process (Tran et al., 2022). Importantly too, the R_L values were higher in Pb(II) ion adsorption at different temperatures compared to MB indicating that PG-NiONPs were more favourable towards Pb(II) adsorption. According to Freundlich isotherm, the n_F values fall in the range of 1 to 10, indicating a favourable interaction between the nanoadsorbent and the MB/

Table 4
Comparison of PG-NiONPs for MB and Pb(II) adsorption with the different nanoadsorbents over the literature.

Adsorbent	Surface area (m^2/g)	Adsorption capacity (mg/g)		Isotherm model	Kinetic model	Initial Conc. (mg/L)	pH	Contact time (min)	Adsorbent mass (mg/L)	Temp. (K)	Reusability	Reference
		MB	Pb(II)									
S-ZrON	–	23.26	nd	Langmuir	PSO*	20	10	300	300	313	3	(Alagarsamy et al., 2022)
$Na_2Ti_3O_7$	159.63	250.62	nd	Langmuir	PSO	50	nd	10	10	RT	nd	(Reyes-Miranda et al., 2021)
CP-ACFs	1826	461.80	nd	Langmuir	PSO	1000	7	180	50	298	nd	(Liu et al., 2021)
CuO-NPAC	262.35	464.20	nd	Sips	PSO	50	9	180	4000	318	7	(Prajapati and Mondal, 2020)
Fe-BP	57.30	28.10	nd	Langmuir	PSO	5	nd	48	2500	318	nd	(Çatlıoğlu et al., 2021)
L2-MNP	nd	234.27	nd	Langmuir	PSO	150	7	1440	750	298	10	(Du et al., 2022a)
FeMn-HNTs	nd	96.47	nd	Langmuir	PSO	100	7	120	1000	303	5	(Zhang et al., 2020)
Nano GO	nd	429.49	nd	Freundlich	PSO	5	8	15	10	313	nd	(Soudagar et al., 2022)
MFMPAC	458	437.78	182.45	Freundlich	PSO	50	7	60	20	298	6	(Ebadollahzadeh and Zabihi, 2020)
Fe_3O_4@Al–B	117.53	18.59	29.88	nd	PSO	10	5	MB(30)Pb (II) (60)	MB(0.50)Pb (II) (0.83)	298	3	(Ghohestani et al., 2022)
APHGS	nd	249.33	345.93	Langmuir	PSO	MB (100) Pb(II) (200)	MB (7) Pb (II) (5)	1440	1000	313.15	5	(Tang et al., 2022)
DES/GO-Fe_3O_4	nd	nd	120.50	Freundlich	PSO	150	–	180	1	293	nd	(Mehrabi et al., 2020)
BC-MnO_3	181.90	nd	351.37	Langmuir	PSO	150	4.5	1440	25	298	7	(H. Zhang et al., 2020)
$SrCo_2Fe_{16}O_{27}$	nd	nd	0.01	Temkin	PSO	10	9	90	2	298	1	(Varnosfaderani et al., 2022)
Fe_3O_4@TiO_2-CN	nd	nd	92.60	Langmuir	PSO	250	6	60	40	318	**7**	(Mousavi et al., 2019)
HT-NPs	nd	nd	169.49	Langmuir	PSO	700	7	10	5000	298	**5**	(Kim et al., 2021b)
Fe_3O_4-FP	85.69	nd	27.86	Freundlich	PSO	20	7	15	4	298	**4**	(Karami et al., 2022)
CSC@SDBC	53.16	nd	228.69	Redlich-Peterson	PSO	50	5.5	60	nd	303	**5**	(Ifthikar et al., 2020)
IL@MSN	1073	nd	256.40	Freundlich	PSO	50	6	90	1000	298	**nd**	(Firmansyah et al., 2022)
PG-NiONPs	85.40	495.58	508.56	Toth	PSO	100	MB (6) Pb (II) (5)	60	40	323	8	This study

NB: * refers to Pseudo-second order and nd indicate not determined.

Pb(II). In this study, the three parameters models, such as Toth, Sips and Redlich-Peterson a combined form of both Langmuir and Freundlich isotherm models that represents both monolayer and multilayer adsorption characteristics (Jain et al., 2022). It was observed that the exponents of the Toth, Sips and Redlich-Peterson were close to one, thus indicating that the adsorption of MB and Pb(II) ion by PG-NiONPs was more Langmuir in nature (Jain et al., 2022).

3.3.7. Adsorption thermodynamics

The nature of MB and Pb(II) adsorption by PG-NiONPs was investigated through the variations of the equilibrium conditions at the temperatures of 298, 303, 308, 313, 318 and 323 K to provide relevant information on the temperature dependence of the adsorption process and the thermodynamics parameters such as a standard change in Gibbs energy (ΔG°, kJ/mol), enthalpy (ΔH°, kJ/mol), and entropy (ΔS°, kJ/mol K). The calculation of the ΔG°, ΔH°, ΔS° and K_c was explored by Eqs. (14), (15), (S3) and (S4) (Egbosiuba et al., 2020a; Egbosiuba et al., 2020b; Salvestrini and Bollinger, 2022; Tang et al., 2022; Tao et al., 2022; Tran et al., 2022).

$$\Delta G^{\circ} = -RTInK_c \tag{14}$$

$$In\,K_c = -\left(\frac{\Delta H^{\circ}}{R}\right)\frac{1}{T} + \left(\frac{\Delta S^{\circ}}{R}\right) \tag{15}$$

where T (K) refers to the absolute temperature, R (J/mol/K) denotes the universal gas constant, K_c represents the thermodynamic constant at equilibrium. The values of the ΔH° and ΔS° were determined from the Van't Hoff plot of In K_c vs 1/T, as the slope $(-(\Delta S^{\circ}/R))$ and intercept

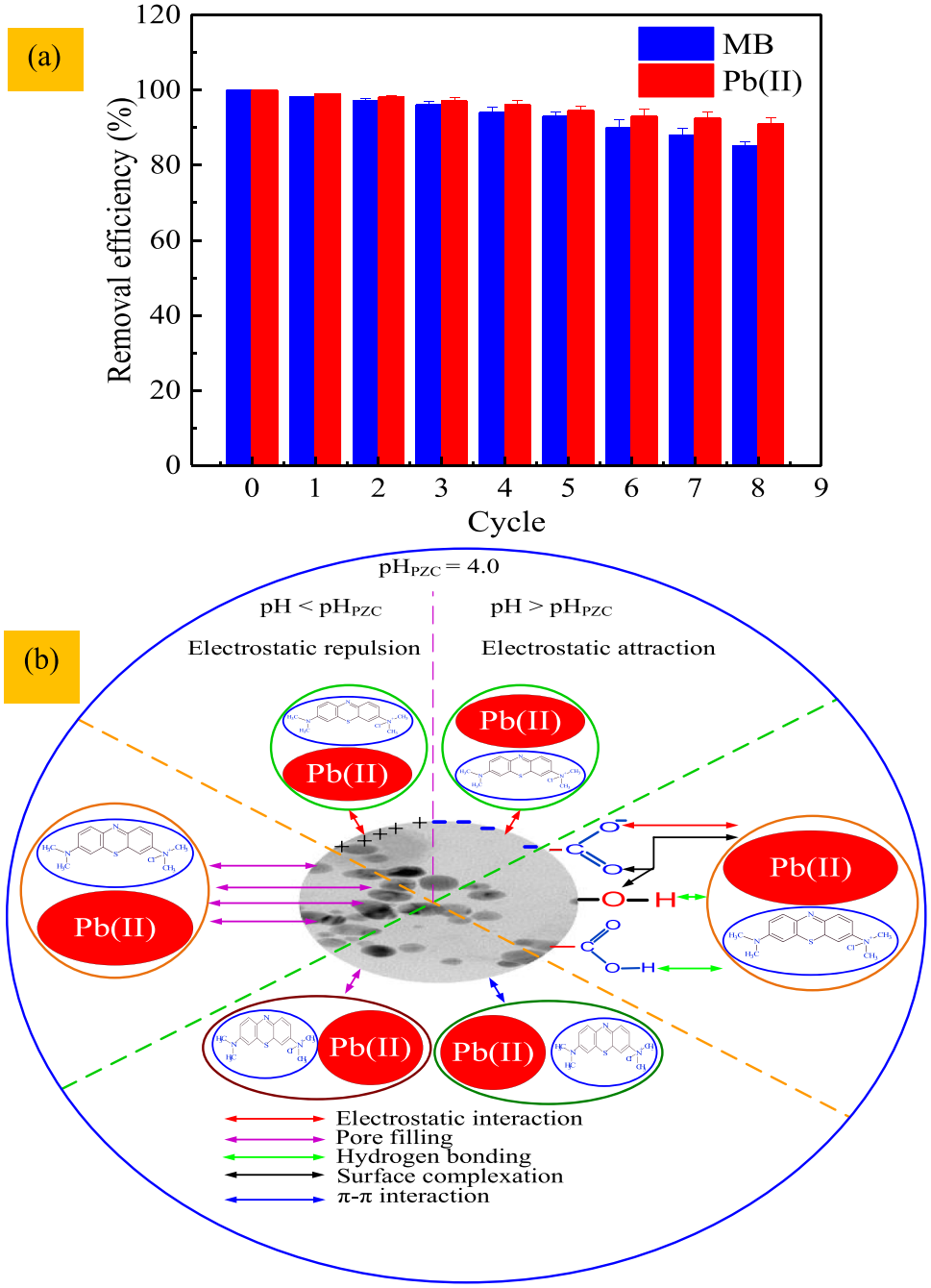

Fig 6. Recycling of PG-NiONPs for the adsorption of MB and Pb(II); (b) Proposed adsorption mechanism for the removal of MB and Pb(II).

$(\Delta S^{\circ}/R)$.

The obtained fitting curve of In K_c vs 1/T is presented in Fig. 4f, while the corresponding thermodynamic parameters for the adsorption of MB and Pb(II) by PG-NiONPs are presented in Table S1. As can be seen in Table S1, all the values of ΔG° are negative ($\Delta G^{\circ} < 0$) at various temperatures for both MB and Pb(II) adsorption, suggesting the favorability, the spontaneity and the practicability of the adsorption process. In addition, the observed decreasing values of ΔG° as the temperature increase is an indication of favourable adsorption of MB and Pb(II) at elevated temperatures using PG-NiONPs. The positive values of ΔH° and ΔS° infer the endothermic nature of the adsorption process and the randomization increment at the nanoadsorbent-adsorbate interface during the removal of MB and Pb(II) ion. Remarkably too, the ΔH° values of 108.62 and 81.74 kJ/mol obtained for MB and Pb(II) ion was higher than the recommended range of 1 to 40 kJ/mol for physisorption controlled adsorption process (Egbosiuba et al., 2020a; Egbosiuba et al., 2020b). Therefore, the adsorption of MB and Pb(II) ion by PG-NiONPs in this study was chemisorption controlled.

3.3.8. Recyclability and stability

Recyclable nanoadsorbents are desirable in practical applications due to the reduction in production cost, disposal of waste and generation of secondary pollutants (Tao et al., 2022). Due to the importance of desorption effectiveness in the regeneration of adsorbents, various eluents including NaOH, HCl, acetone and ethanol have been widely employed to desorb adsorbates from the adsorbent (Tran et al., 2022). In this study, the recyclability of PG-NiONPs was examined through the successive adsorption–desorption experimental cycle using mixtures of NaOH (1 M) and HCl (1 M) as the desorption media due to their desorption effectiveness, cost efficiency and simplicity. According to the reusability results shown in Fig. 6a, the synthesized PG-NiONPs maintained MB and Pb(II) adsorption rates of over 85 and 90 % after eight adsorption cycles. Above all, the observed decrease in the adsorption efficiency of the PG-NiONPs after each desorption may be attributed to the residual Pb(II) and MB that occupied the few adsorption sites (Tao et al., 2022). The results indicate that PG-NiONPs possess remarkable recyclability for MB and Pb(II) adsorption.

Furthermore, the stability of PG-NiONPs was investigated by obtaining the surface properties of the reused nanoadsorbents by XRD and HRSEM techniques. As can be seen in Fig. S1, the major XRD diffraction peaks of PG-NiONPs were maintained after eight adsorption–desorption cycles, except for the weaker intensity of the peaks and the appearance of two smaller peaks at 20.62° and 26.90°, respectively. According to Fig. S2, the surface morphology of the PG-NiONPs did not show any noticeable variation after the eight adsorption–desorption cycles, revealing that the surface properties of the nanoadsorbents did not undergo any significant change after the reusability evaluation. Therefore, it can be concluded that green synthesized PG-NiONPs remain a potentially highly reusable and stable nanoadsorbent for the removal of MB and Pb(II) from wastewater.

3.3.9. Comparison of nanoadsorbents and limitations

To compare the adsorption performance of green PG-NiONPs with previous similar nanoadsorbents, some parameters and experimental conditions such as BET surface area, adsorption capacity, initial adsorbate concentration, pH, equilibrium contact time, adsorbent mass, temperature and reusability were considered as presented in Table 4. It was noticed that green PG-NiONPs exhibited enhanced adsorption capacity compared to different other nanoadsorbents such as metallic nanoparticles composites, functionalized metallic nanoparticles, functionalized carbon nanotubes, graphene oxide and metal–organic frameworks from previous studies. Also, the nanoadsorbent mass of 40 mg/L was relatively small compared to higher amounts of 5000, 4000, 2500, 1000 and 750 mg/L reported previously (Çatlıoğlu et al., 2021; Du et al., 2022a; Kim et al., 2021a; Prajapati and Mondal, 2020; Tang et al., 2022), thus practically saving the quantity of nanoadsorbents usage. Particularly, the reusability capacity of PG-NiONPs up to 8 adsorption cycles implies the cost-effectiveness of the nanoadsorbents compared to so many other materials. Importantly too, the equilibrium contact time for the MB and Pb(II) adsorption by green PG-NiONPs was just 60 min, indicating a minimized time-consuming treatment time for the adsorbates. From the comparative results, it can be justifiably recommended that PG-NiONPs is a potential nanoadsorbent for the MB and Pb(II) treatment in real wastewater.

On the other hand, several potential study limitations can be discussed here. This research is currently in the first stages of laboratory-scale tests. It is recommended that the pilot experiments on the application of green PG-NiONPs nanoadsorbent be conducted to assess the viability, applicability, and overall cost of the real treatment process. Additionally, there isn't a thorough discussion of what happens to PG-NiONPs after the final reuse. The most popular technique for disposing of spent PG-NiONPs nanoadsorbents to prevent secondary pollution may be incineration, although other approaches including conversion to new catalysts and new electronic materials based on the circular economy are also possible. Finally, it is anticipated that future research will enhance the performance of PG-NiONPs as reliable nanoadsorbents and broaden their applications as catalysts, sensors, and systems for drug delivery.

3.3.10. Adsorption mechanism

The chemical characteristics of MB and Pb(II) make them cationic dyes and metals, which means that positively charged ions are produced when dissolved in water. The point of zero charges (pH_{PZC}) can be determined to clarify if these cations interact electrostatically with the surface of the PG-NiONPs. The surface charge property of PG-NiONPs prepared using *Psidium guajava* leaves extract was measured by the pHpzc technique and a value of 4.0 was shown in Fig. 6b. Specifically, the result indicates that PG-NiONPs revealed a positively charged surface at pH lower than 4.0, but negatively charged at pH values greater than 4.0. Therefore, PG-NiONPs can interact electrostatically with the cations of MB and Pb(II) by increasing the effectiveness of adsorption. The best results at pH 6 and 5 for MB and Pb(II) in Fig. 4a provide strong support for this theory. However, the observed decline in the adsorption capacity of MB and Pb(II) beyond pH 6 and 5 indicate that electrostatic interactions are insufficient to account for this result and additional mechanisms outside electrostatic interactions may also play a major role.

The adsorption of MB and Pb(II) can be influenced by the presence of certain factors, such as hydrogen bonding, surface complexation and pores filling. One or more organic molecules may be present on the surface of PG-NiONPs due to their synthesis using natural compounds in *Psidium guajava* leaves extract. Some functional groups, including carboxyl groups (–COOH), hydroxyl groups (–OH) and carbonyl groups (C-O) were discovered following FTIR spectra. Through hydrogen bonding, these functional groups may interact with the functional groups of the adsorbate for possible adsorption. The MB and Pb(II) molecules can interact with the porous active surfaces of PG-NiONPs through pores adsorption and surface complexation. However, subsequent research should thoroughly examine the adsorption mechanism of MB and Pb(II) over PG-NiONPs.

3.4. Conclusion and future directions

In this study, natural phytochemicals isolated from *Psidium guajava* leaves extract were successfully used to synthesize green PG-NiONPs for the adsorption of MB dye and Pb(II) ions in wastewater. Using XRD, FTIR, HRSEM, EDX, HRTEM, and N_2 adsorption–desorption isotherm measurement, green PG-NiONPs were thoroughly characterized for functional groups, crystal structure, morphological structure, microstructures and surface properties. MB and Pb(II) ions adsorption was optimized at pH (6 for MB and 5 for Pb(II)), contact time (60 min),

nanoadsorbent mass (40 mg/L) and temperature (50 °C). Toth isotherm model best fitted the experimental data ahead of the Redlich-Peterson, Langmuir, Freundlich and Sips model. The kinetics revealed a matching fitting of the pseudo-second-order kinetic model compared to the pseudo-first-order, Elovich and intraparticle diffusion kinetic model. The maximum adsorption capacity for MB and Pb(II) adsorption by green PG-NiONPs was determined as 495.58 and 508.56 mg/g, respectively. Green PG-NiONPs have a high adsorption capacity than and can be recycled for at least eight times. The possible MB and Pb(II) adsorption mechanisms were identified as electrostatic interaction, pores filling, hydrogen bonding, surface complexation and π-π interaction. Based on outstanding dye and metal ions adsorption effectiveness, good stability and reusability capacity, the study investigates the enormous potential of green PG-NiONPs to effectively remove dyes and metal ions contaminants from wastewater. In addition to helping to fabricate next-generation nanoadsorbents, this study also paves the way for a promising future research directions.

CRediT authorship contribution statement

Dominic Chukwu Onu: Conceptualization, Investigation, Methodology, Data curation, Writing – original draft, Writing – review & editing, Validation. **Akinpelu Kamoru Babayemi:** Investigation, Methodology, Data curation, Writing – original draft, Writing – review & editing. **Titus Chinedu Egbosiuba:** Investigation, Methodology, Data curation, Writing – original draft, Writing – review & editing, Validation. **Blessing Onyinye Okafor:** Data curation, Methodology, Software. **Ijeoma Jacinta Ani:** Data curation, Writing – review & editing. **Saheed Mustapha:** Data curation, Methodology, Software. **Jimoh Oladejo Tijani:** Resources, Supervision. **Wisdom Chukwuemeke Ulakpa:** Writing – review & editing, Methodology, Data curation. **Prosper Eguono Ovuoraye:** Data curation, Methodology, Software. **Ambali Saka Abdulkareem:** Data curation, Writing – review & editing.

Declaration of Competing Interest

The authors declare that they have no known competing financial interests or personal relationships that could have appeared to influence the work reported in this paper.

Data availability

Data will be made available on request.

Appendix A. Supplementary data

Supplementary data to this article can be found online at https://doi.org/10.1016/j.enmm.2023.100818.

References

Abdulkareem, A.S., Hamzat, W.A., Tijani, J.O., Egbosiuba, T.C., Mustapha, S., Abubakre, O.K., Okafor, B.O., Babayemi, A.K., 2023. Isotherm, kinetics, thermodynamics and mechanism of metal ions adsorption from electroplating wastewater using treated and functionalized carbon nanotubes. J. Environ. Chem. Eng. 11 (1), 109180.

Adel, M., Ahmed, M.A., Elabiad, M.A., Mohamed, A.A., 2022. Removal of heavy metals and dyes from wastewater using graphene oxide-based nanomaterials: A critical review. Environ. Nanotechnology, Monit. Manag. 18, 100719 https://doi.org/10.1016/j.enmm.2022.100719.

Ahmed, S.F., Mofijur, M., Nuzhat, S., Chowdhury, A.T., Rafa, N., Uddin, M.A., Inayat, A., Mahlia, T.M.I., Ong, H.C., Chia, W.Y., Show, P.L., 2021. Recent developments in physical, biological, chemical, and hybrid treatment techniques for removing emerging contaminants from wastewater. J. Hazard. Mater. 416, 125912 https://doi.org/10.1016/j.jhazmat.2021.125912.

Alagarsamy, A., Chandrasekaran, S., Manikandan, A., 2022. Green synthesis and characterization studies of biogenic zirconium oxide (ZrO2) nanoparticles for adsorptive removal of methylene blue dye. J. Mol. Struct. 1247, 131275 https://doi.org/10.1016/j.molstruc.2021.131275.

Ali, T., Warsi, M.F., Zulfiqar, S., Sami, A., Ullah, S., Rasheed, A., Alsafari, I.A., Agboola, P.O., Shakir, I., Baig, M.M., 2022. Green nickel/nickel oxide nanoparticles for prospective antibacterial and environmental remediation applications. Ceram. Int. 48, 8331–8340. https://doi.org/10.1016/j.ceramint.2021.12.039.

Aliyu, S., Ambali, A.S., Oladejo, T.J., Mustapha, S., Egbosiuba, T.C., Bada, S.O., 2023. Development of Ag-doped on multi-walled carbon nanotubes for the treatment of fish pond effluent. Reg. Stud. Mar. Sci. 58, 102797 https://doi.org/10.1016/j.rsma.2022.102797.

Aragaw, T.A., Alene, A.N., 2022. A comparative study of acidic, basic, and reactive dyes adsorption from aqueous solution onto kaolin adsorbent : Effect of operating parameters, isotherms, kinetics, and thermodynamics. Emerg. Contam. 8, 59–74. https://doi.org/10.1016/j.emcon.2022.01.002.

Bhaumik, M., Maity, A., Brink, H.G., 2021. Zero valent nickel nanoparticles decorated polyaniline nanotubes for the efficient removal of Pb(II) from aqueous solution: Synthesis, characterization and mechanism investigation. Chem. Eng. J. 417, 127910 https://doi.org/10.1016/j.cej.2020.127910.

Bouabid, K., Lamchouri, F., Toufik, H., El, M., Faouzi, A., 2020. Phytochemical investigation, in vitro and in vivo antioxidant properties of aqueous and organic extracts of toxic plant: Atractylis gummifera L. J. Ethnopharmacol. 112640 https://doi.org/10.1016/j.jep.2020.112640.

Çatlıoğlu, F., Akay, S., Turunç, E., Gözmen, B., Anastopoulos, I., Kayan, B., Kalderis, D., 2021. Preparation and application of Fe-modified banana peel in the adsorption of methylene blue: Process optimization using response surface methodology. Environ. Nanotechnology, Monit. Manag. 16, 100517.

Doan, V.D., Phung, M.T., Nguyen, T.L.H., Mai, T.C., Nguyen, T.D., 2020. Noble metallic nanoparticles from waste Nypa fruticans fruit husk: Biosynthesis, characterization, antibacterial activity and recyclable catalysis. Arab. J. Chem. 13, 7490–7503. https://doi.org/10.1016/j.arabjc.2020.08.024.

Du, B., Bai, Y., Pan, Z., Xu, J., Wang, Q., Wang, X., Lv, G., Zhou, J., 2022a. pH fractionated lignin for the preparation of lignin-based magnetic nanoparticles for the removal of methylene blue dye. Sep. Purif. Technol. 295, 121302 https://doi.org/10.1016/j.seppur.2022.121302.

Du, B., Chai, L., Li, W., Wang, X., Chen, X., Zhou, J., Sun, R.-C., 2022b. Preparation of functionalized magnetic graphene oxide/lignin composite nanoparticles for adsorption of heavy metal ions and reuse as electromagnetic wave absorbers. Sep. Purif. Technol. 297, 121509.

Ebadollahzadeh, H., Zabihi, M., 2020. Competitive adsorption of methylene blue and Pb (II) ions on the nano-magnetic activated carbon and alumina. Mater. Chem. Phys. 248, 122893 https://doi.org/10.1016/j.matchemphys.2020.122893.

Egbosiuba, T.C., 2022a. Application of Agricultural Waste in Anionic Dyes Removal from Wastewater. In: Muthu, S.S., Khadir, A. (Eds.), Textile Wastewater Treatment. Sustainable Textiles: Production, Processing, Manufacturing & Chemistry. Springer, Singapore, pp. 111–141. https://doi.org/10.1007/978-981-19-2852-9_7.

Egbosiuba, T.C., 2022b. Incorporation of zero-valent silver and polyvinyl acetate on the surface matrix of carbon nanotubes for the adsorption of mercury and chromium from industrial wastewater. Niger. J. Technol. 41, 158–168. https://doi.org/10.4314/njt.v41i1.20.

Egbosiuba, T.C., 2022c. Biochar and bio-oil fuel properties from nickel nanoparticles assisted pyrolysis of cassava peel. Heliyon 8 (8), e10114.

Egbosiuba, T.C., Abdulkareem, A.S., 2021. Highly efficient as-synthesized and oxidized multi-walled carbon nanotubes for copper(II) and zinc(II) ion adsorption in a batch and fixed-bed process. J. Mater. Res. Technol. 15, 2848–2872. https://doi.org/10.1016/j.jmrt.2021.09.094.

Egbosiuba, T.C., Abdulkareem, A.S., Kovo, A.S., Afolabi, E.A., Tijani, J.O., Auta, M., Roos, W.D., 2020a. Ultrasonic enhanced adsorption of methylene blue onto the optimized surface area of activated carbon: Adsorption isotherm, kinetics and thermodynamics. Chem. Eng. Res. Des. 153, 315–336.

Egbosiuba, T.C., Abdulkareem, A.S., Kovo, A.S., Afolabi, E.A., Tijani, J.O., Roos, W.D., 2020b. Enhanced adsorption of As(V) and Mn(VII) from industrial wastewater using multi-walled carbon nanotubes and carboxylated multi-walled carbon nanotubes. Chemosphere 254, 126780. https://doi.org/10.1016/j.chemosphere.2020.126780.

Egbosiuba, T.C., Abdulkareem, A.S., Kovo, A.S., Afolabi, E.A., Tijani, J.O., Bankole, M.T., Bo, S., Roos, W.D., 2021a. Adsorption of Cr(VI), Ni(II), Fe(II) and Cd(II) ions by KIAgNPs decorated MWCNTs in a batch and fixed bed process. Sci. Rep. 11, 1–20. https://doi.org/10.1038/s41598-020-79857-z.

Egbosiuba, T.C., Abdulkareem, A.S., Tijani, J.O., Ani, J.I., Krikstolaityte, V., Srinivasan, M., Veksha, A., Lisak, G., 2021b. Taguchi optimization design of diameter-controlled synthesis of multi walled carbon nanotubes for the adsorption of Pb(II) and Ni(II) from chemical industry wastewater. Chemosphere 266, 128937. https://doi.org/10.1016/j.chemosphere.2020.128937.

Egbosiuba, T.C., Egwunyenga, M.C., Tijani, J.O., Mustapha, S., Abdulkareem, A.S., Kovo, A.S., Krikstolaityte, V., Veksha, A., Wagner, M., Lisak, G., 2022. Activated multi-walled carbon nanotubes decorated with zero valent nickel nanoparticles for arsenic, cadmium and lead adsorption from wastewater in a batch and continuous flow modes. J. Hazard. Mater. 423, 126993 https://doi.org/10.1016/j.jhazmat.2021.126993.

Ekeleme, K., Tsaku, P., Nkene, I., Ufomadu, U., Abimiku, R., Oti, V., Sidi, M., 2017. Phytochemical analysis and antibacterial activity of Psidium guajava L. leaf extracts. GSC Biol. Pharm. Sci. 1, 013–019. https://doi.org/10.30574/gscbps.2017.1.2.0024.

Ezhilarasi, A.A., Vijaya, J.J., Kaviyarasu, K., Zhang, X., Kennedy, L.J., 2020. Green synthesis of nickel oxide nanoparticles using Solanum trilobatum extract for cytotoxicity, antibacterial and photocatalytic studies. Surfac. Interf. 20, 100553 https://doi.org/10.1016/j.surfin.2020.100553.

Fernández, I., González-Mora, J.L., Lorenzo-Luis, P., Villalonga, R., Salazar-Carballo, P. A., 2020. Nickel oxide nanoparticles-modified glassy carbon electrodes for non-

enzymatic determination of total sugars in commercial beverages. Microchem. J. 159, 105538.
Firmansyah, M.L., Hassan, N.S., Jalil, A.A., Mukti, R.R., Teh, L.P., Setiabudi, H.D., 2022. Structural investigation of phosphonium-based ionic liquid impregnated mesostructured silica nanoparticles and application towards the adsorption of Pb(II). Chem. Eng. Res. Des. 178, 328–339. https://doi.org/10.1016/j.cherd.2021.12.025.
Gebretinsae, H.G., Tsegay, M.G., Nuru, Z.Y., 2019. Biosynthesis of nickel oxide (NiO) nanoparticles from cactus plant extract. Mater. Today Proc. 36, 566–570. https://doi.org/10.1016/j.matpr.2020.05.331.
Ghazal, S., Akbari, A., Hosseini, H.A., Sabouri, Z., Forouzanfar, F., Khatami, M., Darroudi, M., 2020. Sol-gel biosynthesis of nickel oxide nanoparticles using Cydonia oblonga extract and evaluation of their cytotoxicity and photocatalytic activities. J. Mol. Struct. 1217, 128378 https://doi.org/10.1016/j.molstruc.2020.128378.
Ghohestani, E., Samari, F., Yousefinejad, S., 2022. An efficient removal of methylene blue and lead(II) from aqueous solutions by green synthesized iron oxide/pillared bentonite nanocomposite. Mater. Chem. Phys. 287, 126266 https://doi.org/10.1016/j.matchemphys.2022.126266.
Goel, R., Jha, R., Ravikant, C., 2020. Investigating the structural, electrochemical, and optical properties of p-type spherical nickel oxide (NiO) nanoparticles. J. Phys. Chem. Solids 144, 109488. https://doi.org/10.1016/j.jpcs.2020.109488.
Gómez-Avilés, A., Peñas-Garzón, M., Belver, C., Rodriguez, J.J., Bedia, J., 2022. Equilibrium, kinetics and breakthrough curves of acetaminophen adsorption onto activated carbons from microwave-assisted FeCl3-activation of lignin. Sep. Purif. Technol. 278, 119654.
Hashemzadeh, F., Ariannezhad, M., Derakhshandeh, S.H., 2022. Evaluation of Cephalexin and Amoxicillin removal from aqueous media using activated carbon produced from Aloe vera leaf waste. Chem. Phys. Lett. 800, 139656 https://doi.org/10.1016/j.cplett.2022.139656.
Ifthikar, J., Shahib, I.I., Sellaoui, L., Jawad, A., Zhao, M., Chen, Z., Chen, Z., 2020. pH tunable anionic and cationic heavy metal reduction coupled adsorption by thiol cross-linked composite: Physicochemical interpretations and fixed-bed column mathematical model study. Chem. Eng. J. 401, 126041.
Jain, M., Khan, S.A., Sahoo, A., Dubey, P., Pant, K.K., Ziora, Z.M., Blaskovich, M.A.T., 2022. Statistical evaluation of cow-dung derived activated biochar for phenol adsorption: Adsorption isotherms, kinetics, and thermodynamic studies. Bioresour. Technol. 352, 127030 https://doi.org/10.1016/j.biortech.2022.127030.
Karami, K., Ramezanpour, A., Moradi, N., Sillanpää, M., bayat, P., 2022. Adsorption of Pb(II) ions from aqueous solutions by magnetite (Fe3O4) nanoparticles functionalized with two different Schiff base ligands. J. Mol. Struct. 1271, 134059.
Karpagavinayagam, P., Emi Princess Prasanna, A., Vedhi, C., 2020. Eco-friendly synthesis of nickel oxide nanoparticles using Avicennia Marina leaf extract: Morphological characterization and electrochemical application. Mater. Today Proc. 48, 136–142. https://doi.org/10.1016/j.matpr.2020.04.183.
Kavand, M., Eslami, P., Razeh, L., 2020. The adsorption of cadmium and lead ions from the synthesis wastewater with the activated carbon: Optimization of the single and binary systems. J. Water Process Eng. 34, 101151 https://doi.org/10.1016/j.jwpe.2020.101151.
Khare, P., Patel, R.K., Sharan, S., Shankar, R., 2021. Recent trends in advanced oxidation process for treatment of recalcitrant industrial effluents. In: Advanced Oxidation Processes for Effluent Treatment Plants. Elsevier Inc., pp. 137–160
Khodair, Z.T., Ibrahim, N.M., Kadhim, T.J., Mohammad, A.M., 2022. Synthesis and characterization of nickel oxide (NiO) nanoparticles using an environmentally friendly method, and their biomedical applications. Chem. Phys. Lett. 797, 139564 https://doi.org/10.1016/j.cplett.2022.139564.
Kim, M.S., Jang, H., Baek, S.D., Yoon, S.Y., Kim, S., Lee, S., Lee, J.H., Song, J., Myoung, J. M., 2021b. Highly dispersible surface-modified magnesium oxide nanoparticle-acrylate nanocomposites as a transparent OLED encapsulation material. Prog. Org. Coatings 154, 1–7. https://doi.org/10.1016/j.porgcoat.2021.106196.
Kim, H.J., Lee, J.M., Choi, J.H., Kim, D.H., Han, G.S., Jung, H.S., 2021a. Synthesis and adsorption properties of gelatin-conjugated hematite (α-Fe2O3) nanoparticles for lead removal from wastewater. J. Hazard. Mater. 416, 125696 https://doi.org/10.1016/j.jhazmat.2021.125696.
Kovo, A.S., Alaya-Ibrahim, S., Abdulkareem, A.S., Adeniyi, O.D., Egbosiuba, T.C., Tijani, J.O., Saheed, M., Okafor, B.O., Yusuff, A.S., 2023. Column adsorption of biological oxygen demand, chemical oxygen demand and total organic carbon from wastewater by magnetite nanoparticles-zeolite A composite. Heliyon 9 (2), e13095.
Kumar, N.S., Sarbon, N.M., Rana, S.S., Chintagunta, A.D., Prathibha, S., Ingilala, S.K., Jeevan Kumar, S.P., Sai Anvesh, B., Dirisala, V.R., 2021. Extraction of bioactive compounds from Psidium guajava leaves and its utilization in preparation of jellies. AMB Express 11. https://doi.org/10.1186/s13568-021-01194-9.
Kunatsa, Y., Chidewe, C., Zvidzai, C.J., 2020. Phytochemical and anti-nutrient composite from selected marginalized Zimbabwean edible insects and vegetables. J. Agric. Food Res. 2, 100027 https://doi.org/10.1016/j.jafr.2020.100027.
Lingamdinne, L.P., Yang, J.K., Chang, Y.Y., Koduru, J.R., 2016. Low-cost magnetized Lonicera japonica flower biomass for the sorption removal of heavy metals. Hydrometallurgy 165, 81–89. https://doi.org/10.1016/j.hydromet.2015.10.022.
Lingamdinne, L.P., Singh, J., Choi, J.S., Chang, Y.Y., Yang, J.K., Karri, R.R., Koduru, J.R., 2018. Multivariate modeling via artificial neural network applied to enhance methylene blue sorption using graphene-like carbon material prepared from edible sugar. J. Mol. Liq. 265, 416–427. https://doi.org/10.1016/j.molliq.2018.06.022.
Lingamdinne, L.P., Vemula, K.R., Chang, Y.Y., Yang, J.K., Karri, R.R., Koduru, J.R., 2020. Process optimization and modeling of lead removal using iron oxide nanocomposites generated from bio-waste mass. Chemosphere 243, 125257. https://doi.org/10.1016/j.chemosphere.2019.125257.
Lingamdinne, L.P., Godlaveeti, S.K., Angaru, G.K.R., Chang, Y.Y., Nagireddy, R.R., Somala, A.R., Koduru, J.R., 2022. Highly efficient surface sequestration of Pb2+ and Cr3+ from water using a Mn3O4 anchored reduced graphene oxide: Selective removal of Pb2+ from real water. Chemosphere 299, 134457. https://doi.org/10.1016/j.chemosphere.2022.134457.
Lingamdinne, L.P., Amelirad, O., Koduru, J.R., Karri, R.R., Chang, Y.Y., Dehghani, M.H., Mubarak, N.M., 2023. Functionalized bentonite for removal of Pb(II) and As(V) from surface water: Predicting capability and mechanism using artificial neural network. J. Water Process Eng. 51, 103386 https://doi.org/10.1016/j.jwpe.2022.103386.
Lingaraju, K., Raja Naika, H., Nagabhushana, H., Jayanna, K., Devaraja, S., Nagaraju, G., 2020. Biosynthesis of Nickel oxide Nanoparticles from Euphorbia heterophylla (L.) and their biological application. Arab. J. Chem. 13, 4712–4719. https://doi.org/10.1016/j.arabjc.2019.11.003.
Liu, B., Du, C., Chen, J.J., Zhai, J.Y., Wang, Y., Li, H.L., 2021. Preparation of well-developed mesoporous activated carbon fibers from plant pulp fibers and its adsorption of methylene blue from solution. Chem. Phys. Lett. 771, 138535.
Mehrabi, N., Abdul Haq, U.F., Reza, M.T., Aich, N., 2020. Application of deep eutectic solvent for conjugation of magnetic nanoparticles onto graphene oxide for lead(II) and methylene blue removal. J. Environ. Chem. Eng. 8 (5), 104222.
Mousavi, S.V., Bozorgian, A., Mokhtari, N., Gabris, M.A., Rashidi Nodeh, H., Wan Ibrahim, W.A., 2019. A novel cyanopropylsilane-functionalized titanium oxide magnetic nanoparticle for the adsorption of nickel and lead ions from industrial wastewater: Equilibrium, kinetic and thermodynamic studies. Microchem. J. 145, 914–920. https://doi.org/10.1016/j.microc.2018.11.048.
Mustapha, S., Tijani, J.O., Egbosiuba, T.C., Sumaila, A., Amigun, T.A., Salihu, A.B., Ibrahim, Y.O., Ndamitso, M.M., Abdulkareem, S.A., 2022. Sol–gel Synthesis of Kaolin/TiO2 Nanocomposites for Photocatalytic Degradation of Tannery Wastewater, in: Karchiyappan, T., Karri, R.R., Dehghani, M.H. (Eds.), Industrial Wastewater Treatment . Water Science and Technology Library, Vol 106. Springer, Cham, pp. 23–42. Doi: 10.1016/B978-0-12-409548-9.10167-8.
Mustapha, S., Tijani, J.O., Egbosiuba, T.C., Taiwo, A.A., Abdulkareem, S.A., Sumaila, A., Ndamitso, M.M., Ayodesi, U.N., 2023. Removal of Pollutants from Wastewater Through Nanofiltration: A Review. In: Ahmad, A., Alshammari, M.B. (Eds.), Nanofiltration Membrane for Water Purification. Springer, Singapore, pp. 247–273 https://doi.org/https://doi.org/10.1007/978-981-19-5315-6_13.
Noukelag, S.K., Razanamahandry, L.C., Ntwampe, S.K.O., Arendse, C.J., Maaza, M., 2021. Industrial dye removal using bio-synthesized Ag-doped ZnO nanoparticles. Environ. Nanotechnology, Monit. Manag. 16, 100463 https://doi.org/10.1016/j.enmm.2021.100463.
Nwanya, A.C., Ndipingwi, M.M., Ikpo, C.O., Obodo, R.M., Nwanya, S.C., Botha, S., Ezema, F.I., Iwuoha, E.I., Maaza, M., 2020. Zea mays lea silk extract mediated synthesis of nickel oxide nanoparticles as positive electrode material for asymmetric supercabattery. J. Alloys Compd. 822, 153581 https://doi.org/10.1016/j.jallcom.2019.153581.
Oncho, D.A., Ejigu, M.C., Urgessa, O.E., 2021. Phytochemical constituent and antimicrobial properties of guava extracts of east Hararghe of Oromia. Ethiopia. Clin. Phytoscience 7. https://doi.org/10.1186/s40816-021-00268-2.
Onukwuli, O.D., Nnaji, P.C., Menkiti, M.C., Anadebe, V.C., Oke, E.O., Ude, C.N., Ude, C. J., Okafor, N.A., 2021. Dual-purpose optimization of dye-polluted wastewater decontamination using bio-coagulants from multiple processing techniques via neural intelligence algorithm and response surface methodology. J. Taiwan Inst. Chem. Eng. 125, 372–386.
Prabhu, S., Daniel Thangadurai, T., Vijai Bharathy, P., Kalugasalam, P., 2022. Synthesis and characterization of nickel oxide nanoparticles using Clitoria ternatea flower extract: Photocatalytic dye degradation under sunlight and antibacterial activity applications. Results Chem. 4, 100285 https://doi.org/10.1016/j.rechem.2022.100285.
Prajapati, A.K., Mondal, M.K., 2020. Comprehensive kinetic and mass transfer modeling for methylene blue dye adsorption onto CuO nanoparticles loaded on nanoporous activated carbon prepared from waste coconut shell. J. Mol. Liq. 307, 112949 https://doi.org/10.1016/j.molliq.2020.112949.
Reyes-Miranda, J., Garcia-Murillo, A., Garrido-Hernández, A., Carrillo-Romo, F., de, J., 2021. Fast and mild alkaline solvothermal synthesis of nanostructured flower-like Na2Ti3O7 and its methylene blue adsorption capacity. Mater. Lett. 292, 129589 https://doi.org/10.1016/j.matlet.2021.129589.
Riaz, T., Munnwar, A., Shahzadi, T., Zaib, M., Shahid, S., Javed, M., Iqbal, S., Rizwan, K., Waqas, M., Khalid, B., Awwad, N.S., Ibrahium, H.A., Bajaber, M.A., 2022. Phyto-mediated synthesis of nickel oxide (NiO) nanoparticles using leaves' extract of Syzygium cumini for antioxidant and dyes removal studies from wastewater. Inorg. Chem. Commun. 142, 109656.
Roy, H., Islam, M.S., Arifin, M.T., Firoz, S.H., 2022. Chitosan-ZnO decorated Moringa oleifera seed biochar for sequestration of methylene blue: Isotherms, kinetics, and response surface analysis. Environ. Nanotechnol., Monit. Manag. 18, 100752 https://doi.org/10.1016/j.enmm.2022.100752.
Sagadevan, S., Fatimah, I., Egbosiub, T.C., Alshahateet, S.F., Lett, J.A., Weldegebrieal, G. K., Le, M.V., Johan, M.R., 2022. Photocatalytic Efficiency of Titanium Dioxide for Dyes and Heavy Metals Removal from Wastewater. Bull. Chem. React. Eng. Catal. 17, 430–450. https://doi.org/10.9767/BCREC.17.2.13948.430-450.
Salvestrini, S., Bollinger, J.-C., 2022. Revisiting the extended van't Hoff equation: Comments on "Highly-efficient nitrogen self-doped biochar for versatile dyes'' removal prepared from soybean cake via a simple dual-templating approach and associated thermodynamics"". J. Clean. Prod. 373, 133632.
Sellaoui, L., Mendoza-Castillo, D.I., Reynel-Ávila, H.E., Ávila-Camacho, B.A., Díaz-Muñoz, L.L., Ghalla, H., Bonilla-Petriciolet, A., Lamine, A.B., 2019. Understanding the adsorption of Pb2+, Hg2+ and Zn2+ from aqueous solution on a lignocellulosic biomass char using advanced statistical physics models and density functional theory simulations. Chem. Eng. J. 365, 305–316. https://doi.org/10.1016/j.cej.2019.02.052.

Soudagar, S., Akash, S., Sree Venkat, M., Rao Poiba, V., Vangalapati, M., 2022. Adsorption of methylene blue dye on nano graphene oxide-thermodynamics and kinetic studies. Mater. Today Proc. 59, 667–672. https://doi.org/10.1016/j.matpr.2021.12.199.

Tang, Q., Zhang, F., Chen, W., Ma, D., Du, B., Zhang, K., Huang, X., Luo, H., Fan, L., An, X., Zhang, X., Cheng, L., Wei, Z., Zheng, H., 2022. Floating-separation adsorbent for methylene blue and Pb(II) removal: Structure construction and adsorption mechanism. Sep. Purif. Technol. 295, 121332 https://doi.org/10.1016/j.seppur.2022.121332.

Tao, Y.u., Yang, B., Wang, F., Yan, Y., Hong, X., Xu, H., Xia, M., Wang, F., 2022. Green synthesis of MOF-808 with modulation of particle sizes and defects for efficient phosphate sequestration. Sep. Purif. Technol. 300, 121825.

Tijani, J.O., Abdullahi, M.N., Bankole, M.T., Mustapha, S., Egbosiuba, T.C., Ndamitso, M. M., Abdulkareem, A.S., Muzenda, E., 2021. Photocatalytic and toxicity evaluation of local dyeing wastewater by aluminium/boron doped WO3 nanoparticles. J. Water Process Eng. 44, 102376 https://doi.org/10.1016/j.jwpe.2021.102376.

Tijani, J.O., Odeh, E.I., Mustapha, S., Egbosiuba, T.C., Daniel, A.I., Abdulkareem, A.S., Muya, F.N., 2022. Photocatalytic, electrochemical, antibacterial and antioxidant behaviour of carbon-sulphur Co-doped zirconium (IV) oxide nanocomposite. Clean. Chem. Eng. 3, 100034 https://doi.org/10.1016/j.clce.2022.100034.

Tran, T.V., Nguyen, D.T.C., Kumar, P.S., Din, A.T.M., Qazaq, A.S., Vo, D.-V., 2022. Green synthesis of Mn3O4 nanoparticles using Costus woodsonii flowers extract for effective removal of malachite green dye. Environ. Res. 214, 113925.

Uko, C.A., Tijani, J.O., Abdulkareem, S.A., Mustapha, S., Egbosiuba, T.C., Muzenda, E., 2022. Adsorptive properties of MgO/WO3 nanoadsorbent for selected heavy metals removal from indigenous dyeing wastewater. Process Saf. Environ. Prot. 162, 775–794. https://doi.org/10.1016/j.psep.2022.04.057.

Varnosfaderani, N.A., Shoushtari, M.Z., Mousavi Ghahfarokhi, S.E., 2022. SrCo2Fe16O27 nanoparticles for lead ions adsorption process from water. Phys. B Condens. Matter 638, 413859. https://doi.org/10.1016/j.physb.2022.413859.

Varughese, A., Kaur, R., Singh, P., 2020. Green Synthesis and Characterization of Copper Oxide Nanoparticles Using Psidium guajava Leaf Extract. IOP Conf. Ser. Mater. Sci. Eng. 961 (1), 012011.

Venugopal, G., 2017. Green synthesis of silver nanoparticles from Psidium guajava leaves and its antibacterial activity. Int. J. Bioassays 6, 5441. https://doi.org/10.21746/ijbio.2017.07.003.

Wang, Z., Bin Kang, S., Won, S.W., 2022b. Polyethylenimine-aminated polyvinyl chloride fiber for adsorption of reactive dyes from single and binary component systems: Adsorption kinetics and isotherm studies. Colloid. Surf. A Physicochem. Eng. Asp. 647, 128983 https://doi.org/10.1016/j.colsurfa.2022.128983.

Wang, J., Guo, X., 2020. Adsorption kinetic models: Physical meanings, applications, and solving methods. J. Hazard. Mater. 390, 122156 https://doi.org/10.1016/j.jhazmat.2020.122156.

Wang, K., Wang, Y., Zhang, S., di Chen, Y., Wang, R., Ho, S.H., 2022a. Tailoring a novel hierarchical cheese-like porous biochar from algae residue to boost sulfathiazole removal. Environ. Sci. Ecotechnology 10, 100168. https://doi.org/10.1016/j.ese.2022.100168.

Yadav, B.S., Dasgupta, S., 2022. Effect of time, pH, and temperature on kinetics for adsorption of methyl orange dye into the modified nitrate intercalated MgAl LDH adsorbent. Inorg. Chem. Commun. 137, 109203 https://doi.org/10.1016/j.inoche.2022.109203.

Yan, S., Ren, X., Zhang, F., Huang, K., Feng, X., Xing, P., 2022. Comparative study of Pb 2 +, Ni 2 +, and methylene blue adsorption on spherical waste solid-based geopolymer adsorbents enhanced with carbon nanotubes. Sep. Purif. Technol. 284, 120234 https://doi.org/10.1016/j.seppur.2021.120234.

Yimin, D., Jiaqi, Z., Danyang, L., Lanli, N., Liling, Z., Yi, Z., Xiaohong, Z., 2018. Preparation of Congo red functionalized Fe3O4@SiO2 nanoparticle and its application for the removal of methylene blue. Colloids Surf. A Physicochem. Eng. Asp. 550, 90–98. https://doi.org/10.1016/j.colsurfa.2018.04.033.

Zahra, T., Ahmad, K.S., 2020. Structural, optical and electrochemical studies of organo-templated wet synthesis of cubic shaped nickel oxide nanoparticles. Optik (Stuttg). 205, 164241 https://doi.org/10.1016/j.ijleo.2020.164241.

Zayed, M., Othman, H., Ghazal, H., Hassabo, A.G., 2021. Psidium Guajava leave extract as reducing agent for synthesis of zinc oxide nanoparticles and its application to impart multifunctional properties for cellulosic fabrics. Biointerface Res. Appl. Chem. 11, 13535–13556. https://doi.org/10.33263/BRIAC115.1353513556.

Zhang, G., Li, L., Zhou, G., Lin, Z., Wang, J., Wang, G., Ling, F., Liu, T., 2022. Recyclable aminophenylboronic acid modified bacterial cellulose microspheres for tetracycline removal: Kinetic, equilibrium and adsorption performance studies for hoggery sewer. Environ. Pollut. 307, 119544.

Zhang, H., Xu, F., Xue, J., Chen, S., Wang, J., Yang, Y., 2020. Enhanced removal of heavy metal ions from aqueous solution using manganese dioxide-loaded biochar: Behavior and mechanism. Sci. Rep. 10, 1–13. https://doi.org/10.1038/s41598-020-63000-z.

Zhang, Q., Xu, S., Li, Y., Ding, P., Zhang, Y., Zhao, P., 2021. Green-synthesized nickel oxide nanoparticles enhances biohydrogen production of Klebsiella sp. WL1316 using lignocellulosic hydrolysate and its regulatory mechanism. Fuel 305, 121585. https://doi.org/10.1016/j.fuel.2021.121585.